

## A SEARCH FOR H I LYMAN $\alpha$ COUNTERPARTS TO ULTRA-FAST X-RAY OUTFLOWS

GERARD A. KRISS<sup>1</sup>, JULIA C. LEE<sup>2</sup> AND ASHKBIZ DANEHKAR<sup>3</sup>

*Accepted for publication in Apj, 04/16/2018*

### ABSTRACT

Prompted by the H I Ly $\alpha$  absorption associated with the X-ray ultra-fast outflow at  $-17\,300\text{ km s}^{-1}$  in the quasar PG 1211+143, we have searched archival UV spectra at the expected locations of H I Ly $\alpha$  absorption for a large sample of ultra-fast outflows identified in *XMM-Newton* and *Suzaku* observations. Sixteen of the X-ray outflows have predicted H I Ly $\alpha$  wavelengths falling within the bandpass of spectra from either the *Far Ultraviolet Spectroscopic Explorer* or the *Hubble Space Telescope*, although none of the archival observations were simultaneous with the X-ray observations in which UFOs were detected. In our spectra broad features with full-width at half-maximum of  $1000\text{ km s}^{-1}$  have  $2\text{-}\sigma$  upper limits on the H I column density of generally  $\lesssim 2 \times 10^{13}\text{ cm}^{-2}$ . Using grids of photoionization models covering a broad range of spectral energy distributions, we find that producing Fe XXVI Ly $\alpha$  X-ray absorption with equivalent widths  $> 30\text{ eV}$  and associated H I Ly $\alpha$  absorption with  $N_{\text{HI}} < 2 \times 10^{13}\text{ cm}^{-2}$  requires total absorbing column densities  $N_{\text{H}} > 5 \times 10^{22}\text{ cm}^{-2}$  and ionization parameters  $\log \xi \gtrsim 3.7$ . Nevertheless, a wide range of SEDs would predict observable H I Ly $\alpha$  absorption if ionization parameters are only slightly below peak ionization fractions for Fe XXV and Fe XXVI. The lack of Ly $\alpha$  features in the archival UV spectra indicates that either the UFOs have very high ionization parameters, very hard UV-ionizing spectra, or that they were not present at the time of the UV spectral observations due to variability.

*Keywords:* galaxies: active — galaxies: nuclei — galaxies: Seyfert

### 1. INTRODUCTION

All contemporary models of galaxy evolution require significant levels of feedback initiated by active galactic nuclei (AGN) at the galaxy center (Dubois et al. 2013; Anglés-Alcázar et al. 2017; Beckmann et al. 2017; Nelson et al. 2015). The energy deposited by these fast, massive winds impacts the structure of the host galaxy’s interstellar medium and can have profound influence on star formation through mechanisms that expel gas from the galaxy, heat the interstellar medium, and prevent the formation of giant molecular clouds and star-forming regions (Faucher-Giguère et al. 2013). While much of the feedback that limits galaxy growth can be attributed to star formation (Hopkins et al. 2014), it is AGN feedback that provides the link between galaxy growth and the supermassive black holes at the centers of galaxies (Silk & Rees 1998; King 2003; Ostriker et al. 2010; Soker 2010; Faucher-Giguère & Quataert 2012; Zubovas & Nayakshin 2014; Thompson et al. 2015). Making this link requires coupling much of the binding energy of the central black hole to the host galaxy. Outflows must tap into as much as 0.5% (Hopkins & Elvis 2010) to 5% (Di Matteo et al. 2005) of the AGN bolometric luminosity to generate the correlation between black hole mass and galaxy bulge properties (Ferrarese & Merritt 2000; Gebhardt et al. 2000).

The outflows most intensively studied in local AGN, the X-ray warm absorbers and associated UV ab-

sorption features (Crenshaw et al. 2003) typically have too little kinetic power to meet the above criteria (Crenshaw & Kraemer 2012). However, the ultra-fast X-ray outflows (UFOs) now being detected in both local and distant AGN (Tombesi et al. 2010, 2014, 2015; Gofford et al. 2013; Nardini et al. 2015; Longinotti et al. 2015; Parker et al. 2017) could provide the necessary energy input. These UFOs are characterized by velocities in excess of  $10\,000\text{ km s}^{-1}$  and high column densities of gas, often exceeding  $10^{22}\text{--}10^{23}\text{ cm}^{-2}$ , which would provide sufficient mass and kinetic energy to influence the evolution of the host galaxy (Pounds et al. 2003; Tombesi et al. 2010; Tombesi & Cappi 2014; King & Pounds 2015; Tombesi et al. 2017).

Most UFOs are detected only via a single feature near rest energies of 7 keV, suggesting that they are Lyman  $\alpha$  or He  $\alpha$  features of Fe XXVI or Fe XXV. This lack of spectral features makes secure identification difficult, as well as establishing the precise physical conditions in the outflow. Some lower ionization UFOs do show multiple spectral features affording spectral diagnostics, in particular the multi-component UFO in the Seyfert 1 galaxy IRAS 17020+4544 (Longinotti et al. 2015) (with velocities in the range of  $23\,000\text{--}30\,000\text{ km s}^{-1}$ ), and the quasar PG 1211+143 (Danehkar et al. 2018), with an outflow velocity of  $-17\,300\text{ km s}^{-1}$ . Even more significantly, the outflow in PG 1211+143 has a UV counterpart, with a broad ( $\sim 1000\text{ km s}^{-1}$ ) feature detected in H I Ly $\alpha$  at  $v_{\text{out}} = -16\,980\text{ km s}^{-1}$  (Kriss et al. 2018).

Given the high ionization of most UFOs, it is important to determine under what conditions other spectral diagnostics (such as UV absorption lines) are visible. Fukumura et al. (2010) showed that outflows detected via Fe XXV He $\alpha$  can also produce C IV absorption in the UV if the X-ray to optical luminosity ratio is low enough,

<sup>1</sup> Space Telescope Science Institute, 3700 San Martin Drive, Baltimore, MD 21218, USA

<sup>2</sup> Harvard University, John A. Paulson School of Engineering & Applied Science, 29 Oxford Street, Cambridge, MA 02138, USA

<sup>3</sup> Harvard-Smithsonian Center for Astrophysics, 60 Garden Street, Cambridge, MA 02138, USA

e.g.,  $\alpha_{ox} \sim 2$ . Similarly, Hagino et al. (2017) produced a model for the outflow in the  $z = 3.912$  quasar APM 08279+5255 which has both UV and X-ray absorption. Again, this quasar has a low X-ray to optical luminosity ratio,  $\alpha_{ox} = 1.7$ . Significantly, PG 1211+143 shows only H I Ly $\alpha$  and no other UV absorption lines due to its higher X-ray to optical luminosity ratio ( $\alpha_{ox} = 1.46$ ) (Kriss et al. 2018).

It is important to establish under what conditions that gas driving the bulk of an X-ray UFO can produce both X-ray and UV absorption features. If the conditions required for the outflow to be dominated by Fe XXV or Fe XXVI preclude strong Ly $\alpha$  (or features due to other UV ions), then the presence of UV absorption lines may be an important diagnostic of clumpiness in the gas, where higher-density, lower ionization-parameter gas is associated with the X-ray outflow. On the other hand, if any detected UV absorption features are compatible with physical conditions in a homogeneous wind, then UV spectra provide additional diagnostics of its physical conditions and kinematics. Spurred by the detection of the H I Ly $\alpha$  counterpart to the UFO in PG 1211+143, we undertook an archival study of the UV spectra of other X-ray UFOs to search for comparable absorption lines. Our search revealed one possible new counterpart. In this paper we describe the sample of X-ray UFOs we examined, their archival spectra, and a study of photoionization models that can produce both Fe XXV or Fe XXVI and H I Ly $\alpha$  features. We conclude with a discussion of implications for further studies of UFOs.

## 2. THE X-RAY UFO SAMPLE AND ARCHIVAL UV OBSERVATIONS

Our sample of X-ray UFOs is taken from the comprehensive studies of Tombesi et al. (2010) and Gofford et al. (2013). These two surveys are the most uniform, statistically based searches for UFOs in AGN to date. While UFOs have been discovered or suggested in other individual studies, for making a comparison with other wavebands, using these uniformly selected objects enables us to draw more objective conclusions. Among a set of 101 *XMM-Newton* observations of 42 radio-quiet AGN, Tombesi et al. (2010) detected 18 potential Fe XXV or Fe XXVI K $\alpha$  features with outflow velocities  $> 10\,000$  km s $^{-1}$ . Gofford et al. (2013) identified 17 candidate features. Of these 35 candidates, 16 have UV spectra that cover the wavelength range predicted for an H I Ly $\alpha$  counterpart. The remaining candidates, especially the Seyfert 2s, are too heavily reddened to produce detectable UV flux. Several others have outflow velocities placing the predicted wavelength for Ly $\alpha$  outside the spectral range of existing UV observations. The 16 candidates with available UV spectra are listed in Table 1. Most UFOs listed in Table 1 are from Tombesi et al. (2010); those from Gofford et al. (2013) are indicated by footnotes in column (4). When tabulating the UFO outflow velocities, a difference from Tombesi et al. (2010) is that we give the outflow velocity as negative, representing a blue shift. In total, we examined 39 locations in 36 discrete spectra to search for counterparts to the X-ray UFOs.

Most of the UV spectra in our sample are from observations using the *Far Ultraviolet Spectroscopic Explorer* (FUSE) (Moos et al. 2000) since the high outflow ve-

locities shift the predicted wavelength of Ly $\alpha$  to wavelengths generally shorter than 1150 Å. The remaining spectra are from *Hubble Space Telescope* (HST) observations using either the *Space Telescope Imaging Spectrograph* (STIS) (Woodgate et al. 1998) or the *Cosmic Origins Spectrograph* (COS) (Green et al. 2012). Many of the UFO candidates have multiple UV spectra available. Unfortunately, none of the UV spectra were simultaneous with any of the X-ray observations. Both of these aspects are significant, as Kriss et al. (2018) showed that the Ly $\alpha$  counterpart to the  $-17\,300$  km s $^{-1}$  X-ray UFO is variable, and is only detected in the observation obtained simultaneously with the *Chandra* observation of PG 1211+143 (Danekhar et al. 2018).

The UV spectra in our study were downloaded from the *Mikulski Archive for Space Telescopes* (MAST) and can be obtained at 10.17909/T9JQ2K. FUSE spectra cover the wavelength range from 912–1187 Å using four separate mirrors and gratings coated with either LiF or SiC. The MAST data were processed using the final FUSE pipeline (Dixon et al. 2007), but after retrieval, we combined the four separate spectra using a post-processing pipeline that aligned the wavelength scales of all four spectra, normalized their fluxes to the channel whose center was associated with the fine-guidance camera, and combined them into a single spectrum to increase the signal-to-noise (S/N) ratio. These combined spectra were re-binned to 0.05 Å pixels, approximately half a resolution element. The COS spectra downloaded from MAST were also processed using customized techniques to align and merge all central wavelength settings and FP-POS positions (Kriss et al. 2011; De Rosa et al. 2015). The single STIS spectrum (Mrk 766) was used as given by MAST.

## 3. ANALYSIS OF THE SPECTRA

For each of the UV spectra in our sample, we examined the wavelength region surrounding the nominal wavelength for Ly $\alpha$  predicted by the outflow velocity for the candidate UFO. In most cases, a simple linear fit to the continuum was adequate to describe the spectrum in these narrow wavelength intervals. In our analysis we ignored foreground interstellar absorption lines, and potential foreground intergalactic H I Ly $\alpha$  lines. When necessary, we fitted more complicated spectral models including the broad wings of nearby emission lines (e.g., O VI or Ly $\alpha$ ), or other intrinsic emission lines. For our fits we used the task `specfit` (Kriss 1994), and used a criterion of  $\Delta\chi^2 = 3.84$  from the minimum  $\chi^2$  (for one degree of freedom—the EW of the absorption feature) to establish an upper limit at the 2- $\sigma$  confidence level (95%) in the case of non-detections.

Of the 36 spectra we examined, only two show evidence for an absorption feature at the predicted location for H I Ly $\alpha$ . Both are separate FUSE observations of Mrk 79. Although the feature in the FUSE spectra of Mrk 79 is formally significant at a confidence level  $>99.9\%$ , it appears in only one of two FUSE detector segments, and its reality is tentative.

In Figure 1 we show portions of the UV spectrum for each of the objects in our sample in the velocity range surrounding the previously detected X-ray UFO feature. In most cases in which we do not detect any Ly $\alpha$  counter-

**Table 1:** X-ray UFO Sample

Object	IAU Name	Redshift ( $z$ )	$v_{out}$ ( $c$ )	UFO Date	UV Data Set	UV Instrument	UV Date	Exposure (s)
1H0419–577	J042600.7–571202	0.104	–0.037 <sup>a</sup>	2002-09-25	lb4f33030	HST/COS/G130M	2010-06-01	3 750
Ark 120	J051611.4–000859	0.03271	–0.269 <sup>a</sup>	2003-08-24	P1011201	FUSE	2000-11-01	90 000
Mrk 79	J074232.8+494834	0.02219	–0.091 <sup>a</sup>	2006-09-30	P1011701	FUSE	1999-11-30	7 381
		0.02219	–0.091 <sup>a</sup>	2006-09-30	P1011702	FUSE	2000-01-14	11 734
		0.02219	–0.091 <sup>a</sup>	2006-09-30	P1011703	FUSE	2000-02-22	12 499
NGC 4051	J120309.6+443153	0.00233	–0.150 <sup>a</sup>	2002-11-22	C0190101	FUSE	2003-01-18	13 933
		0.00233	–0.150 <sup>a</sup>	2002-11-22	C0190102	FUSE	2003-03-19	28 594
NGC 4151	J121032.6+392421	0.00332	–0.055 <sup>b</sup>	2006-12-18	P1110505	FUSE	2000-03-05	20 610
		0.00332	–0.055 <sup>b</sup>	2006-12-18	P2110201	FUSE	2000-04-08	15 272
		0.00332	–0.055 <sup>b</sup>	2006-12-18	P2110202	FUSE	2002-06-01	6 602
NGC 4151	J121032.6+392421	0.00332	–0.105 <sup>a</sup>	2006-11-29	P1110505	FUSE	2000-03-05	20 610
		0.00332	–0.105 <sup>a</sup>	2006-11-29	P2110201	FUSE	2001-04-08	15 272
		0.00332	–0.105 <sup>a</sup>	2006-11-29	P2110202	FUSE	2002-06-01	6 602
PG 1211+143	J121417.7+140313	0.0809	–0.128 <sup>a</sup>	2001-01-16	lcs501010	HST/COS/G140L	2015-04-12	1 900
		0.0809	–0.128 <sup>a</sup>	2001-01-16	lcs502010	HST/COS/G140L	2015-04-14	1 900
		0.0809	–0.128 <sup>a</sup>	2001-01-16	lcs504010	HST/COS/G140L	2015-04-14	1 900
		0.0809	–0.128 <sup>a</sup>	2001-01-16	P1072001	FUSE	2000-04-25	52 277
Mrk 766	J121826.5+294846	0.01293	–0.044 <sup>a</sup>	2005-05-25	o51502030	HST/STIS/G140L	2000-04-11	2 925
Mrk 205	J122144.2+751838	0.07084	–0.100 <sup>a</sup>	2000-05-07	Q1060203	FUSE	1999-12-29	38 800
		0.07084	–0.100 <sup>a</sup>	2000-05-07	S6010801	FUSE	2002-02-02	18 900
		0.07084	–0.100 <sup>a</sup>	2000-05-07	D0540101	FUSE	2003-11-14	19 618
		0.07084	–0.100 <sup>a</sup>	2000-05-07	D0540102	FUSE	2003-11-17	107 518
		0.07084	–0.100 <sup>a</sup>	2000-05-07	D0540103	FUSE	2003-06-28	18 068
Mrk 279	J135303.4+691829	0.03045	–0.220 <sup>b</sup>	2009-05-14	P1080303	FUSE	1999-12-28	61 139
		0.03045	–0.220 <sup>b</sup>	2009-05-14	P1080304	FUSE	2000-01-11	30 288
		0.03045	–0.220 <sup>b</sup>	2009-05-14	S6010501	FUSE	2002-01-28	18 115
		0.03045	–0.220 <sup>b</sup>	2009-05-14	S6010502	FUSE	2002-01-29	19 082
		0.03045	–0.220 <sup>b</sup>	2009-05-14	C0900201	FUSE	2002-05-18	47 414
		0.03045	–0.220 <sup>b</sup>	2009-05-14	D1540101	FUSE	2003-05-14	91 402
		0.03045	–0.220 <sup>b</sup>	2009-05-14	F3250102 <sup>c</sup>	FUSE	2005-12-06	10 393
Mrk 841	J150401.2+102616	0.03642	–0.034 <sup>a</sup>	2005-07-17	lc8y15010	HST/COS/G130M	2014-07-06	1 740
Mrk 290	J153552.4+575409	0.02958	–0.141 <sup>a</sup>	2006-05-04	P1072901	FUSE	2000-03-16	12 769
		0.02958	–0.141 <sup>a</sup>	2006-05-04	D0760101	FUSE	2000-02-27	9 239
		0.02958	–0.141 <sup>a</sup>	2006-05-04	D0760102	FUSE	2004-03-06	46 055
		0.02958	–0.141 <sup>a</sup>	2006-05-04	E0840101	FUSE	2004-11-07	11 424
Mrk 509	J204409.8–104325	0.0344	–0.172 <sup>a</sup>	2000-10-25	X0170101	FUSE	1999-11-02	19 355
		0.0344	–0.172 <sup>a</sup>	2000-10-25	X0170102	FUSE	1999-11-06	32 457
		0.0344	–0.172 <sup>a</sup>	2000-10-25	P1080601	FUSE	2000-09-05	62 100
Mrk 509	J204409.8–104325	0.0344	–0.141 <sup>a</sup>	2005-10-18	X0170101	FUSE	1999-11-02	19 355
		0.0344	–0.141 <sup>a</sup>	2005-10-18	X0170102	FUSE	1999-11-06	32 457
		0.0344	–0.141 <sup>a</sup>	2005-10-18	P1080601	FUSE	2000-09-05	62 100
Mrk 509	J204409.8–104325	0.0344	–0.196 <sup>a</sup>	2006-04-25	X0170101	FUSE	1999-11-02	19 355
		0.0344	–0.196 <sup>a</sup>	2006-04-25	X0170102	FUSE	1999-11-06	32 457
		0.0344	–0.196 <sup>a</sup>	2006-04-25	P1080601	FUSE	2000-09-05	62 100
MR2251–178	J225405.9–173455	0.06609	–0.137 <sup>b</sup>	2009-05-07	P1111010	FUSE	2001-06-20	54 112

**Notes.** (1) Object name. (2) IAU name (Right Ascension and Declination, J2000 equinox). (3) Redshift. (4) Outflow velocity of the X-ray UFO. (5) Date of the X-ray observation of the UFO. (6) UV data set name. (7) UV instrument used. (8) Date of the UV observation. (9) Exposure time for the UV observation.

<sup>a</sup> UFO detected by Tombesi et al. (2010).

<sup>b</sup> UFO detected by Gofford et al. (2013).

<sup>c</sup> Sum of four exposures, F3250102, F3250103, F3250104, and F3250106.

part, we only show the highest S/N UV spectrum for that object or for the UFO candidate. In some cases, e.g. Mrk 79, in which two spectra show a possible UV counterpart and another one does not, we show all UV spectra. For Mrk 841, a complicated case in which the anticipated location of a UFO counterpart is on the shoulder of strong foreground Milky Way Ly $\alpha$  absorption, we show both the raw spectrum and a normalized model. Finally, for the high velocity ( $v_{out} = -0.128c$ ) UFO in PG 1211+143, for which the FUSE and COS spectra differ significantly in spectral resolution, we also show both spectra. The

best fit linear or powerlaw continuum model in each case is shown as a green line. For illustrative purposes, we also show what a 1 Å equivalent width (EW) absorption line with a full-width-at-half-maximum (FWHM) of 1000 km s<sup>–1</sup> would look like when placed at the location predicted by the UFO outflow velocity. Such a line would be comparable in appearance to the Ly $\alpha$  counterpart detected in PG 1211+143 at  $v_{out} = -16\,980$  km s<sup>–1</sup> by Kriss et al. (2018).

From our fits we either determined upper limits to an absorption feature of assumed FWHM=1000 km s<sup>–1</sup>, or

measured the EW of the detected absorption feature. Given the EW, we also determined an upper limit on the neutral hydrogen column density by integrating the Gaussian profile of the absorption line using the apparent optical depth method of [Savage & Sembach \(1991\)](#). Table 2 gives our measurements for each spectrum.

#### 4. DISCUSSION OF INDIVIDUAL OBJECTS

Each of the sources and the spectra shown in Figure 1 has its own peculiarities. Below we give additional details on the UV spectral properties of the sources and our fits to the archival spectra.

##### 4.1. 1H0419–577

The narrow-line Seyfert 1 1H0419–577 has fairly strong soft X-ray absorption which [Pounds et al. \(2004\)](#) attribute to low-ionization gas internal to the source. [Tombesi et al. \(2013\)](#) characterize this as a warm absorber whose parameters are not well determined. They quote an ionization parameter for this gas of  $\log \xi \sim 1.2$ . This is roughly compatible with the strong, intrinsic UV absorption visible in FUSE and HST spectra. [Edmonds et al. \(2011\)](#) describe three low-velocity outflow systems ranging from  $-50$  to  $-230$  km s $^{-1}$ . The strongest component, at  $-230$  km s $^{-1}$ , has low density  $< 10^3$  cm $^{-3}$ , and is located at 9 kpc, suggesting it is part of a full-scale galactic outflow. Their total spectrum is used in our analysis here.

The two deep, narrow absorption lines at 1286 Å and 1295 Å are unidentified. They are not foreground interstellar features, but we consider them to be likely intervening intergalactic (IGM) absorption. Their equivalent widths of 0.28 Å and 0.13 Å, respectively, and their widths, with Doppler parameters  $b = 33$  and  $b = 44$  km s $^{-1}$ , are typical of H I IGM lines ([Tilton et al. 2012](#)).

##### 4.2. Ark 120

The high velocity of the UFO in Ark 120 places its potential Ly $\alpha$  counterpart near the shortest wavelengths observable with FUSE. Although this spectrum appears to be of poor quality, most of the “noise” one sees in Figure 1b is due to the plethora of foreground interstellar absorption features present at short UV wavelengths. These are marked in red in the figure. Strong Ly $\delta$  and O I airglow are also present at 948 Å and 950 Å. These features and the interstellar absorption lines make it difficult to set a sensitive upper limit on Ly $\alpha$  absorption in this spectrum.

##### 4.3. Mrk 79

This Seyfert 1 has three FUSE observations in the archive. No UV absorption is detectable in the second observation, which has the highest S/N, but the first and third data sets show a broad, shallow depression at the location predicted for the X-ray UFO. Unfortunately, the center of that feature is coincident with the N I  $\lambda 1134$  airglow feature, which is quite prominent in the second observation. Also, thermal misalignments during the third observation led to very low fluxes in the LiF2 channel, so the absorption detected mostly in the LiF1 spectrum cannot be independently confirmed in the LiF2 spectrum.

Although the feature is statistically significant (at a confidence level exceeding 99.9%), we consider its detection tentative.

As with 1H0419–577, Mrk 79 shows strong, variable soft X-ray absorption ([Gallo et al. 2011](#)) due to a warm absorber. In their analysis of the *XMM-Newton* pn spectra, [Gallo et al. \(2011\)](#) find significant variations in the ionization parameter, which is low ( $\log \xi \sim 0.8 - 2.0$ ), and possible variations in the column density. Analysis of the longest *XMM-Newton* RGS spectrum by [Laha et al. \(2014\)](#) similarly finds  $\log \xi \sim 2.0$  and  $\log N_{\text{H}} \sim 21.0$  cm $^{-2}$ . Mrk 79 also has several intrinsic, variable UV absorption features due to O VI and Ly $\beta$  in its FUSE spectrum ([Dunn et al. 2008](#)). These have outflow velocities of  $-320$  and  $-1400$  km s $^{-1}$ , both of which are at lower velocity than the  $< -2400$  km s $^{-1}$  velocity of the warm absorber in the analysis of the 2008 *XMM-Newton* RGS spectrum by [Laha et al. \(2014\)](#).

##### 4.4. NGC 4051

Fortuitously, the predicted location of Ly $\alpha$  in this FUSE spectrum of NGC 4051 lies longward of the wing of O VI emission in this AGN. Narrow, foreground interstellar absorption lines are also present, and they are marked in red in the figure.

##### 4.5. NGC 4151

NGC 4151 contains two suggested UFOs, one at  $v_{\text{out}} = -0.105c$  ([Tombesi et al. 2010](#)), and one at  $v_{\text{out}} = -0.0555c$  ([Gofford et al. 2013](#)). Both have predicted locations for H I Ly $\alpha$  lying in the FUSE band, for which three separate observations are available. The wavelength regions spanned by the predicted wavelengths of a Ly $\alpha$  counterpart contain several narrow absorption features that correspond to foreground interstellar lines, as well as a strong intrinsic absorption line from the metastable levels of C III\*  $\lambda 1176$ . Although there are some large-scale undulations in flux in each of these regions, they are not present in all observations nor in both detector segments, nor do they rise to the level of significance of comparable features seen in the FUSE spectra of Mrk 79.

##### 4.6. PG 1211+143

The prototype for this survey, PG 1211+143 has one UFO at a velocity of  $v_{\text{out}} = -17300$  km s $^{-1}$  ([Danekhar et al. 2018](#)) which is associated with H I Ly $\alpha$  absorption at  $v_{\text{out}} = -16980$  km s $^{-1}$  ([Kriss et al. 2018](#)). In the [Tombesi et al. \(2010\)](#) sample, PG 1211+143, also has another UFO at  $v_{\text{out}} = -0.128c$ , which has been extensively studied ([Pounds 2014](#); [Pounds et al. 2016](#)). We show two spectra of the region of the predicted Ly $\alpha$  counterpart to this higher velocity UFO in Figures 1i and 1j. The illustrated region is spectrally complex, containing weak emission lines of S IV and He II intrinsic to PG 1211+143, as well as foreground interstellar absorption features, which are marked in red in the COS spectrum in Figure 1i. The COS spectrum was taken with grating G140L, which has significantly lower resolution (resolving power  $\sim 2000$ ) than the FUSE spectrum in Figure 1j (resolving power  $\sim 18000$ ), and it is the sum of the three exposures obtained in the combined *Chandra* and *HST* campaign ([Danekhar et al. 2018](#); [Kriss et al. 2018](#)).

**Table 2:** Measurements of H I Ly $\alpha$  Absorption Features for X-ray UFOs

Object	Data Set	$\lambda_o$ ( $\text{\AA}$ )	EW ( $\text{\AA}$ )	FWHM ( $\text{km s}^{-1}$ )	$\log N_{\text{HI}}$ ( $\log \text{cm}^{-2}$ )
1H0419–577	lb4f03030	1293.3	< 0.029	1000	< 12.73
Ark 120	P1011201	952.8	< 0.42	1000	< 13.89
Mrk 79	P1011701	1133.5	1.32	$1000 \pm 200$	14.39
	P1011702	1134.3	< 0.19	1000	< 13.54
	P1011703	1134.3	1.33	$910 \pm 200$	14.39
NGC 4051	C0190101	1047.6	< 0.11	1000	< 13.31
	C0190102	1047.6	< 0.11	1000	< 13.31
NGC 4151	P1110505	1097.7	< 0.079	1000	< 13.16
	P2110201	1097.7	< 0.079	1000	< 13.16
	P2110202	1097.7	< 0.079	1000	< 13.16
NGC 4151	P1110505	1154.4	< 0.072	1000	< 13.12
	P2110201	1154.4	< 0.16	1000	< 13.46
	P2110202	1154.4	< 0.10	1000	< 13.27
PG 1211+143	P1072001	1097.7	< 0.065	1000	< 13.08
	lcs502020 <sup>a</sup>	1097.7	< 0.53	1000	< 14.00
Mrk 766	o5l502030	1178.5	< 1.00	1000	< 14.27
Mrk 205	Q1060203	1077.5	< 0.28	1000	< 13.72
	S6010801	1077.5	< 0.27	1000	< 13.70
	D0540101	1077.5	< 0.25	1000	< 13.67
	D0540102	1077.5	< 0.11	1000	< 13.31
	D0540103	1077.5	< 0.33	1000	< 13.79
Mrk 279	P1080303	1001.6	< 0.11	1000	< 13.29
	P1080304	1001.6	< 0.12	1000	< 13.33
	C0900201	1001.6	< 0.25	1000	< 13.67
	D1540101	1001.6	< 0.054	1000	< 13.00
	S6010501	1001.6	< 0.58	1000	< 14.03
	S6010502	1001.6	< 0.65	1000	< 14.08
	F3250102 <sup>b</sup>	1001.6	< 0.93	1000	< 14.55
Mrk 841	lc8y15010	1217.8	< 0.054	1000	< 13.00
Mrk 290	P1072901	1086.0	< 0.30	1000	< 13.74
	D0760101	1086.0	< 0.38	1000	< 13.85
	D0760102	1086.0	< 0.14	1000	< 13.41
	E0840101	1086.0	< 0.32	1000	< 13.75
Mrk 509	X0170101	1057.0	< 0.053	1000	< 12.99
	X0170102	1057.0	< 0.046	1000	< 12.93
	P1080601	1057.0	< 0.039	1000	< 12.86
Mrk 509	X0170101	1091.1	< 0.074	1000	< 13.14
	X0170102	1091.1	...	1000	...
	P1080601	1091.1	< 0.057	1000	< 13.02
Mrk 509	X0170101	1031.0	< 0.059	1000	< 14.13
	X0170102	1031.0	< 0.051	1000	< 14.13
	P1080601	1031.0	< 0.049	1000	< 14.13
MR2251–178	P1111010	1129.1	< 0.059	1000	< 14.13

<sup>a</sup> Based on sum of all three exposures, lcs501010, lcs502010, and lcs504010.

<sup>b</sup> Based on sum of four exposures, F3250102, F3250103, F3250104, and F3250106.

Neither the FUSE nor the COS spectrum (or the individual exposures in the COS spectrum) shows evidence for broad Ly $\alpha$  absorption.

#### 4.7. Mrk 766

In Tombesi et al. (2010), Mrk 766 has two potential UFOs. The highest-velocity one falls at wavelengths accessible to FUSE, but no FUSE observations of Mrk 766 were performed due to its reddened, faint UV spectrum. The STIS G140L spectrum shown in Figure 1k doesn't set a significantly tight constraint on a potential Ly $\alpha$  feature, both due its low S/N and the low resolution.

#### 4.8. Mrk 205

Observation D0540102 of Mrk 205 is representative of its five separate FUSE observations, none of which show

evidence for any Ly $\alpha$  absorption associated with an X-ray UFO.

#### 4.9. Mrk 279

The spectrum shown in Figure 1m is from the FUSE observations in the extensive UV and X-ray campaign on Mrk 279 (Gabel et al. 2005; Arav et al. 2007; Costantini et al. 2007). Mrk 279 has a complex, low velocity outflow, with UV and X-ray spectral lines spanning velocities from +100 to  $-550 \text{ km s}^{-1}$ . Unfortunately, the broad, blended troughs of intrinsic absorption due to Ly $\gamma$  and C III  $\lambda 977$  in this outflow fall within the region of interest for a Ly $\alpha$  counterpart to the suggested X-ray UFO. This makes it difficult to establish a sensitive upper limit for any Ly $\alpha$  absorption.

4.10. *Mrk 841*

Unfortunately, the predicted location of Ly $\alpha$  in this spectrum falls right on the red wing of the damped Ly $\alpha$  absorption due to foreground neutral hydrogen in the Milky Way. Nevertheless, we have modeled its profile, the surrounding AGN continuum, and the blue wing of the broad Ly $\alpha$  emission line. This model is shown overlaid on the high-quality COS spectrum in Figure 1n. The blue curve in the same panel shows the appearance of the model if a 1 Å equivalent width absorption line with FWHM=1000 km s<sup>-1</sup> is added. It is clear that this deviates significantly from the data. To illustrate this more clearly, Figure 1o shows a normalized spectrum where the deep, broad absorption feature is obviously not a good match to the data. The red line shows the 2- $\sigma$  upper limit feature that can be accommodated by our fit.

4.11. *Mrk 290*

Mrk 290 is a typical example of an AGN with a spectral break in the far UV that extrapolates directly to the soft X-ray (Shang et al. 2005). It also has a complex warm absorber in the X-ray (Zhang et al. 2011) with corresponding UV absorption lines (Zhang et al. 2015) visible in the FUSE spectrum. The predicted location of Ly $\alpha$  falls near the gap in the FUSE LiF1 detector, which is why the S/N drops abruptly at 1085 Å.

4.12. *Mrk 509*

As with many objects in this sample, Mrk 509 has a complex set of intrinsic UV absorption lines associated with a corresponding set of X-ray warm absorbers. The UV absorption spans a velocity range of -400 km s<sup>-1</sup> to +200 km s<sup>-1</sup> (Kriss et al. 2000, 2011), similar to the soft X-ray absorption seen in the X-ray spectrum (Detmers et al. 2011; Kaastra et al. 2012). All the deep, narrow absorption features in Figures 1q–1s are associated either with the intrinsic absorption features in Mrk 509 or foreground interstellar lines.

4.13. *MR2251–178*

The predicted location of Ly $\alpha$  in this FUSE spectrum of MR2251–178 lies on the far wing of broad O VI emission intrinsic to MR2251–178. The narrow absorption lines in the spectrum are foreground interstellar lines. Prominent N I airglow is present at  $\lambda$ 1134.

## 5. PHOTOIONIZATION MODELS

The high ionization states implied for UFOs identified with Fe XXV or Fe XXVI absorption would at first glance suggest that lower-ionization features such as H I Ly $\alpha$ , C IV, or even O VI would not be detectable. However, given the high column densities required to produce detectable Fe XXVI Ly $\alpha$  absorption (total  $N_{\text{H}} > 10^{23}$  cm<sup>-2</sup>) (Tombesi et al. 2011), an ionization fraction for neutral hydrogen of  $10^{-10}$  would still imply a high enough column density ( $> 10^{13}$  cm<sup>-2</sup>) of neutral hydrogen to produce a detectable UV absorption line. To quantify the conditions under which one might see Ly $\alpha$  absorption or other UV absorption lines concurrently with Fe XXVI absorption, we computed a set of photoionization models covering a broad range in spectral energy distribution (SED). Our calculations were

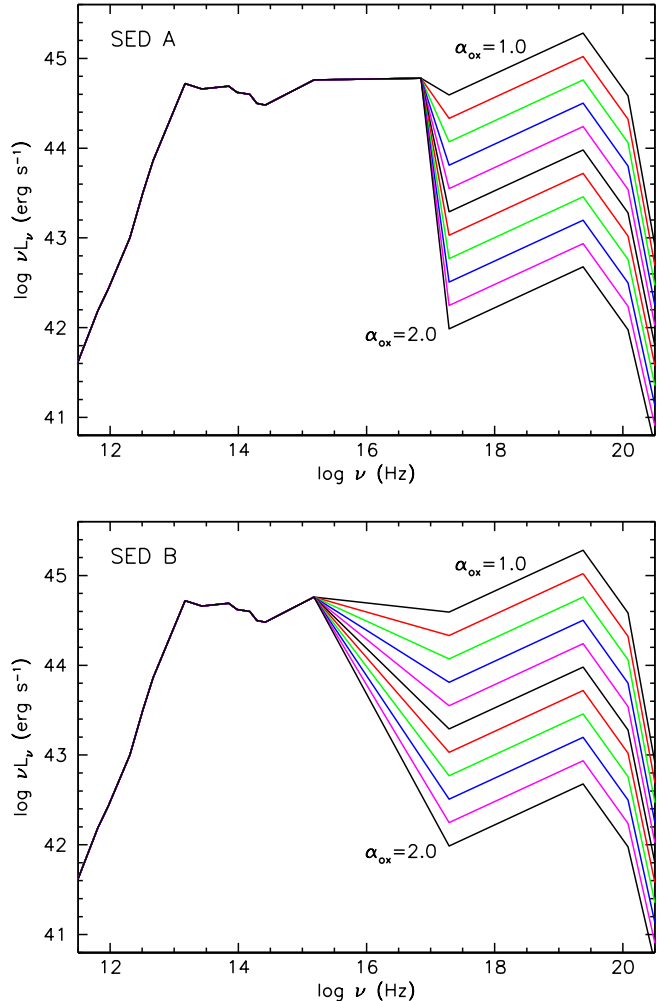


**Figure 2.** : Set of spectral energy distributions used in our photoionization models. SED A has a strong UV ionizing continuum peaking in the extreme ultraviolet. Model SEDs in this shape range in  $\alpha_{\text{ox}}$  from 1.0 to 2.0. The model with  $\alpha_{\text{ox}} = 1.5$  is most similar to the SED of PG 1211+143 used in Danehkar et al. (2018). SED B has a weaker UV ionizing continuum, with a break from a hard power law in the UV to a direct extrapolation to the X-ray power law at 1 keV. Again, model SEDs in this shape range in  $\alpha_{\text{ox}}$  from 1.0 to 2.0.

performed with version 17.00 of CLOUDY, last described by Ferland et al. (2017).

5.1. *Spectral Energy Distributions*

While both Tombesi et al. (2011) and Gofford et al. (2013) generated detailed grids of photoionization models to evaluate their X-ray spectra, their spectral energy distributions were more tailored to their X-ray spectra. The spectral shape in the ionizing ultraviolet is of little consequence for the ionization balance of Fe XXV or Fe XXVI. However, for the purposes of our study, the relative strength and shape of the ionizing ultraviolet spectral range has a large impact on the relative strengths of any UV spectral features that might be associated with

the X-ray outflow. (See the analysis of IRAS13349+2438 by Lee et al. (2013) for a detailed example.) For a baseline spectral energy distribution, we started with the observed SED of PG 1211+143 (Danehkar et al. 2018). As shown in Figure 4 of Danehkar et al. (2018), this SED has a hard ionizing continuum in the extreme ultraviolet, a strong soft X-ray excess, and a typical hard X-ray power law. The UV and extreme UV is characterized by a powerlaw  $f_\nu \sim \nu^{-\alpha}$  with index  $\alpha = 0.99$ , which breaks at 0.25 keV to an index of 5.57 to form the soft X-ray excess. This soft X-ray power law breaks at 0.8 keV to a hard X-ray power law with an energy index of 0.67, which is cut off at 100 keV with a break to an energy index of 2. This spectral shape is similar to the median spectral energy distribution of quasars, e.g., Elvis et al. (1994) or Shang et al. (2011), although the X-ray spectral energy index of 0.67 is slightly harder than the mean of the Tombesi et al. (2010) UFO sample, which Tombesi et al. (2011) give as 0.8.

Starting with this basic shape, and keeping the hard X-ray ( $E > 0.8$  keV) and UV portions of the SED the same (i.e.,  $\alpha = 0.99$  in the UV, and  $\alpha = 0.67$  in the hard X-ray), we adjust the normalization at 0.8 keV to generate a set of SEDs spanning a range in  $\alpha_{ox}$  from 1.0 to 2.0. ( $\alpha_{ox}$  is the effective spectral index from 2500 Å in the UV to 2 keV in the X-ray.) These SEDs are illustrated in the top panel of Figure 2, and they are called “SED A”.

As an alternative, we also explored a set of SEDs that have a much softer spectrum in the hydrogen-ionizing portion of the spectrum. These spectra have a break at the Lyman limit (13.6 eV/912 Å) that extrapolates directly to the soft X-ray at 0.8 keV. Such spectra are typical of many AGN, as illustrated by the  $\sim 1000$  Å breaks seen in composite UV spectra (Zheng et al. 1997; Telfer et al. 2002), and in the spectra of many individual quasars (Shang et al. 2005). These soft spectra are also expected to have higher H I ionization fractions for a comparable level of ionization fractions in X-ray ionic species (Kriss et al. 2018). Again, as for SED A, we generate a set of spectra ranging from 1.0 to 2.0 in  $\alpha_{ox}$  by adjusting the normalization of the hard X-ray spectrum at 0.8 keV. The spectra in the bottom panel of Figure 2 show the spectra representing “SED B”.

### 5.2. X-ray to Optical Luminosity Ratios of the UFO Sample

Our grid of spectral energy distributions allows us to investigate the potential properties of H I Ly $\alpha$  absorption associated with a wide range of spectra. The objects in our particular sample, however, are quite well studied, and so we can examine predictions for each with better precision if we use our knowledge of their individual SEDs. Although we do not produce specific SEDs for each individual object (which would still have the uncertainty of the shape of the unobservable ionizing ultraviolet continuum), we used literature sources and the NASA Extragalactic Database (NED) to obtain X-ray to optical luminosity ratios for each object. We characterize these ratios by the usual effective spectral index from 2500 Å in

the UV to 2 keV in the X-ray, or  $\alpha_{ox}$ . Our preference for selection of values were (1) a fully modeled SED based on simultaneous X-ray and UV observations; (2) values based on simultaneously measured UV and X-ray fluxes; (3) values based on a published SED (but not necessarily modeled using simultaneous observations); (4) values based on median values from NED; (5) a calculation using median values from NED, but inferring a correction for internal absorption in the host galaxy by normalizing the J-band flux from NED to the median radio-quiet SED of Shang et al. (2011). Table 3 gives our adopted  $\alpha_{ox}$  for each source, the method used (1–5 as described above), and the reference for our data. Note that methods 3–5 can lead to uncertainties of  $\sim 0.12$  in  $\alpha_{ox}$  for relative variations in flux between the UV and the X-ray of a factor of 2.

**Table 3:** X-ray to Optical Luminosity Ratios ( $\alpha_{ox}$ ) for the UFO Sample

Object	$\alpha_{ox}$	Method	Reference
1H0419–577	1.24	5	1
Ark 120	1.32	2	2
Mrk 79	1.40	5	1
NGC 4051	1.48	3	3
NGC 4151	1.07	1	4
PG 1211+143	1.47	1	5
Mrk 766	1.38	5	1
Mrk 205	1.13	4	1
Mrk 279	1.19	2	2
Mrk 841	1.36	5	1
Mrk 290	1.31	5	1
Mrk 509	1.31	1	6
MR2251–178	1.14	2	2

References: (1) NED, (2) Laha et al. (2014), (3) Kraemer et al. (2012), (4) Kraemer et al. (2005), (5) Danehkar et al. (2018), (6) Mehdipour et al. (2011).

### 5.3. Photoionization Model Results

Given the SEDs described above, we ran CLOUDY models covering the full range in  $\alpha_{ox}$  for each SED. Each model is characterized by the total hydrogen particle density,  $n_H$  (which is fixed at  $10^{10}$  cm $^{-3}$ ), the total hydrogen column density  $N_H$ , and the ionization parameter  $\xi = L_{ion}/(n_H r^2)$ , where  $L_{ion}$  is the ionizing luminosity integrated from the Lyman limit to 1000 Rydbergs, and  $r$  is the distance from the central source. We used the default CLOUDY solar abundances. As shown in Danehkar et al. (2018), the relevant photoionization solutions are insensitive to densities over the likely density range of  $10^8 - 10^{14}$  cm $^{-3}$ . Each of these models covered a range in ionization parameter  $\xi$  from  $\log \xi = 2.0$  to 5.0 in steps of 0.05 dex. (We ignored lower ranges of  $\xi$  since significant populations of Fe XXV or Fe XXVI, the basis of our study, are not formed at lower values of the ionization parameter.) Given that ionization fronts develop at high column densities and/or low ionization parameters, we found that it is essential to sample the full range of total column density. Therefore, our models also step through a range in the stopping column density from  $\log N_H = 22.0-24.3$  cm $^{-2}$  at 0.1 dex intervals.

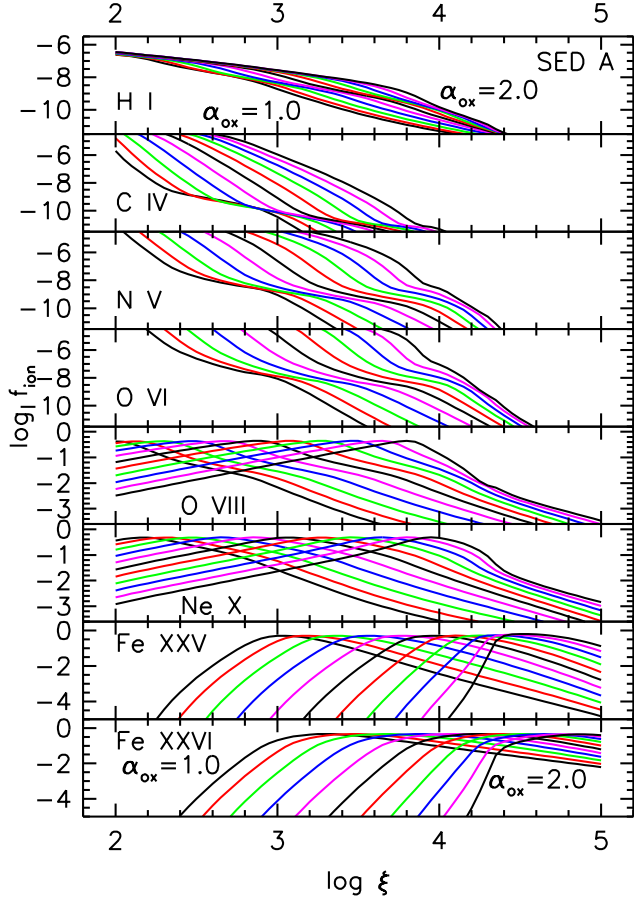


**Figure 3 :** Ionization fractions as a function of ionization parameter for SED A, which has a hard extreme ultraviolet ionizing flux, assuming a total column density of  $\log N_{\text{H}} = 23.0 \text{ cm}^{-2}$ . The alternating color curves span a range in  $\alpha_{\text{ox}}$  from 1.0 to 2.0 at intervals of 0.1.

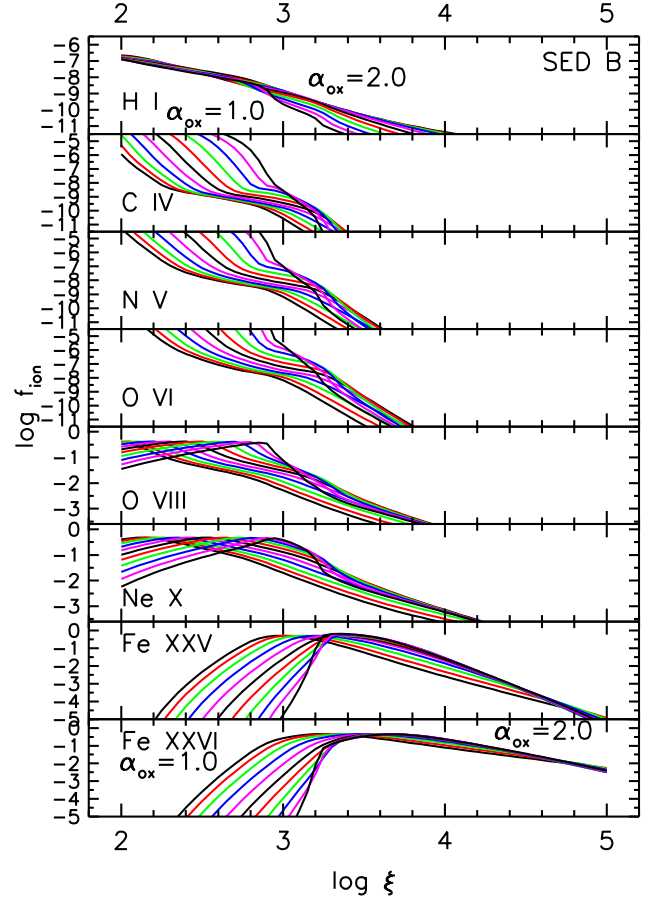


**Figure 4 :** Ionization fractions as a function of ionization parameter for SED B, which has a soft extreme ultraviolet ionizing flux, assuming a total column density of  $\log N_{\text{H}} = 23.0 \text{ cm}^{-2}$ . The alternating color curves span a range in  $\alpha_{\text{ox}}$  from 1.0 to 2.0 at intervals of 0.1.

Figures 3 and 4 show ionization fractions as a function of  $\log \xi$  for the main transitions of interest for our study, H I, C IV, N V, O VI, Fe XXV, and Fe XXVI, computed for a fixed column density of  $\log N_{\text{H}} = 23.0 \text{ cm}^{-2}$ , which is typical of the gas forming Fe XXVI Ly $\alpha$  absorption features (Tombesi et al. 2011). Note the inflections in the fractional ionization curves for the lower-ionization ions that form “ripples” across the figures. These are due to the ionization fronts that develop for higher-ionization ions at ionization parameters that make the calculation ionization bounded for a total column density of  $\log N_{\text{H}} = 23.0 \text{ cm}^{-2}$  for those ions.

We also show representative intermediate ionization states, namely O VIII and Ne X, since lower ionization parameters that favor higher observable columns of H I might also be expected to produce lower-energy X-ray spectral lines easily observed with grating instruments. As anticipated, peak ionization fractions for Fe XXV and Fe XXVI require ionization parameters between  $\log \xi = 3.0$  and 4.5, and corresponding H I ionization fractions are quite low, in the range of  $10^{-8}$  to  $10^{-10}$ . However, as noted earlier, the dominant overall abundance of hy-



drogen can still produce detectable UV absorption lines with column densities of order  $10^{13} \text{ cm}^{-2}$ . C IV, N V, and O VI have higher ionization fractions than hydrogen, but, given that their abundances are lower by factors of several thousand, they ultimately have lower predicted column densities than H I itself.

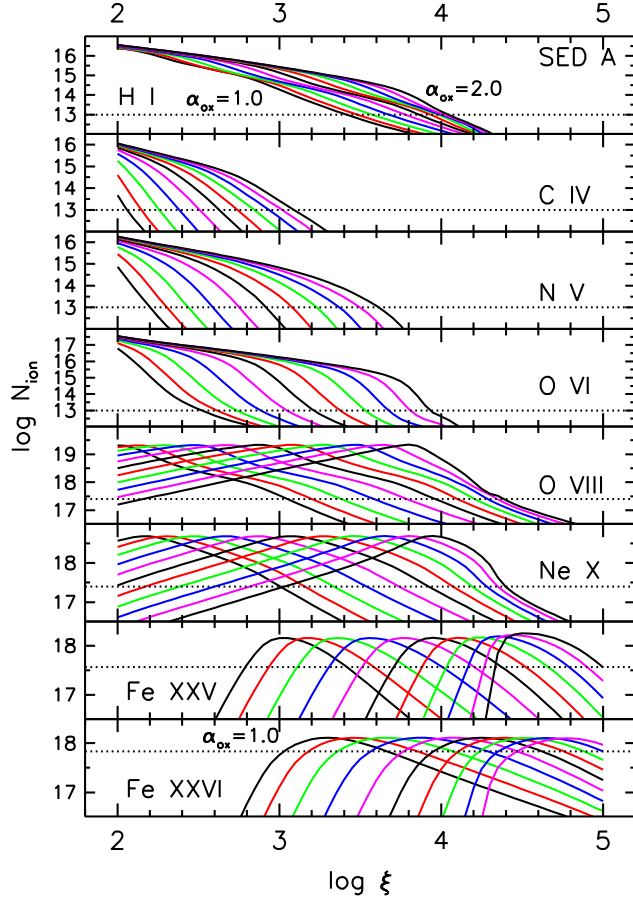


**Figure 5.** : Ionic column densities as a function of ionization parameter for SED A, which has a hard extreme ultraviolet ionizing flux, assuming a total column density of  $\log N_{\text{H}} = 23.0 \text{ cm}^{-2}$ . The alternating color curves span a range in  $\alpha_{\text{ox}}$  from 1.0 to 2.0 at intervals of 0.1. Dashed horizontal lines show approximate thresholds for each ion for detecting UV or X-ray absorption lines (see text).

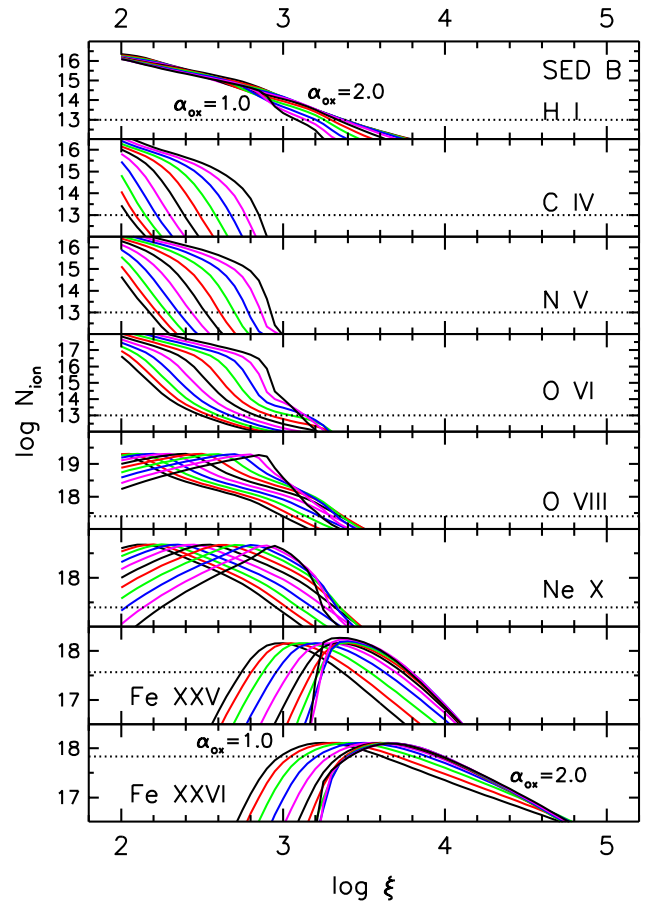


**Figure 6.** : Ionic column densities as a function of ionization parameter for SED B, which has a soft extreme ultraviolet ionizing flux, assuming a total column density of  $\log N_{\text{H}} = 23.0 \text{ cm}^{-2}$ . The alternating color curves span a range in  $\alpha_{\text{ox}}$  from 1.0 to 2.0 at intervals of 0.1. Dashed horizontal lines show approximate thresholds for each ion for detecting UV or X-ray absorption lines (see text).

Figures 5 and 6 show the individual ionic column densities as a function of ionization parameter corresponding to the ionic fractions for a total column density of  $\log N_{\text{H}} = 23.0 \text{ cm}^{-2}$ . To interpret these curves in terms of observable quantities, we must assume a velocity width for the spectral features of interest. Given the  $1000 \text{ km s}^{-1}$  width of the  $\text{Ly}\alpha$  feature in PG 1211+143 (Kriss et al. 2018), at  $\log N_{\text{ion}} < 13.0 \text{ cm}^{-2}$  all UV features are optically thin. H I, C IV, N V and O VI are typically undetectable if  $\log N_{\text{ion}} < 13.0 \text{ cm}^{-2}$ , and these thresholds are indicated in the figures. This breadth must be interpreted as a turbulent velocity. In our photoionization models, temperatures are roughly  $10^6 \text{ K}$ , with a thermal width for H I of  $120 \text{ km s}^{-1}$ , and  $17 \text{ km s}^{-1}$  for Fe. The UFO features in the CCD spectra of Tombesi et al. (2010) and Gofford et al. (2013) are unresolved, and could easily have velocity widths of several thousand  $\text{km s}^{-1}$ . The better studied UFOs in PDS 456 (Reeves et al. 2018) and APM 08279+5255

(Saez & Chartas 2011) are resolved at widths of tens of thousands of  $\text{km s}^{-1}$ . The C IV broad-absorption-line troughs in APM 08279+5255 also have widths of 2000–2500  $\text{km s}^{-1}$ . As one can see in the curves of growth computed by (Tombesi et al. 2011), at line widths above  $\sim 1000 \text{ km s}^{-1}$ , the Fe features are close to optically thin. We will therefore assume they are optically thin for our analysis. At peak ionic fraction for Fe XXVI, given a total column density of  $10^{23} \text{ cm}^{-2}$ , the predicted EW for an Fe XXVI Ly $\alpha$  absorption feature is 55 eV, which is a common strength for many UFOs. Limiting equivalent widths of 30-eV EW in Fe XXV and Fe XXVI require  $\log N_{\text{ion}} = 17.57$  and 17.84, respectively. For O VIII and Ne X, grating observations can usually detect lines with column densities  $\log N_{\text{ion}} > 17.4 \text{ cm}^{-2}$ . Thus, for the soft SED B, if the X-ray UFO absorption feature is Fe XXV or Fe XXVI, one generally would not expect to see any lower ionization features in either the UV or the X-ray except for perhaps Ly $\alpha$ . For the harder SED A, however, one might see lower-ionization X-ray ions such as O VIII and Ne X if  $\alpha_{\text{ox}} < 1.5$ , but again, no UV ions other than Ly $\alpha$  would typically be visible.

Using our grid of photoionization models, we can evaluate the detectability of UV absorption features associated with our sample of UFO outflows. Tables 4 and 5 give predicted H I column densities for each source, given its  $\alpha_{\text{ox}}$  and the EW of its Fe absorption feature. In most cases, the predicted H I column densities are well below the upper limits given in Table 2. However, as one can see in Figures 3 and 4, Fe XXV and Fe XXVI have high ionization fractions extending to much lower ionization parameters than at peak. To ascertain more generally what spectral shapes and ionization parameters would produce both detectable Fe absorption lines and UV absorption lines, we computed the resulting ionic column densities set by the requirements that the EW of Fe XXV or Fe XXVI K $\alpha$  transitions produce an X-ray absorption feature of 30 eV (a typical detection level in Tombesi et al. (2010)). Given these requirements on the Fe column densities, for each ionization parameter in our model grid we identified the corresponding column densities of all other ions in the model grid. The predictions for H I given a 30 eV Fe XXVI feature are shown in Figure 7, and in Figure 8 for Fe XXV. The solid dots in the figure show the column densities predicted at peak ion fractions for Fe XXVI, and crosses give the peak ionization fractions for Fe XXV. These are generally lower than an “easy to detect” limit of  $N_{\text{HI}} = 2 \times 10^{13} \text{ cm}^{-2}$  for a Ly $\alpha$  feature. However, for SEDs at low  $\alpha_{\text{ox}}$  (i.e.,  $\sim 1.2$ ) and lower-than-peak ionization fractions for Fe, Ly $\alpha$  features are certainly detectable. All other UV ions, however, remain at predicted column densities below  $N_{\text{ion}} = 10^{12} \text{ cm}^{-2}$ , which are undetectable; therefore we do not show any curves for these ions.

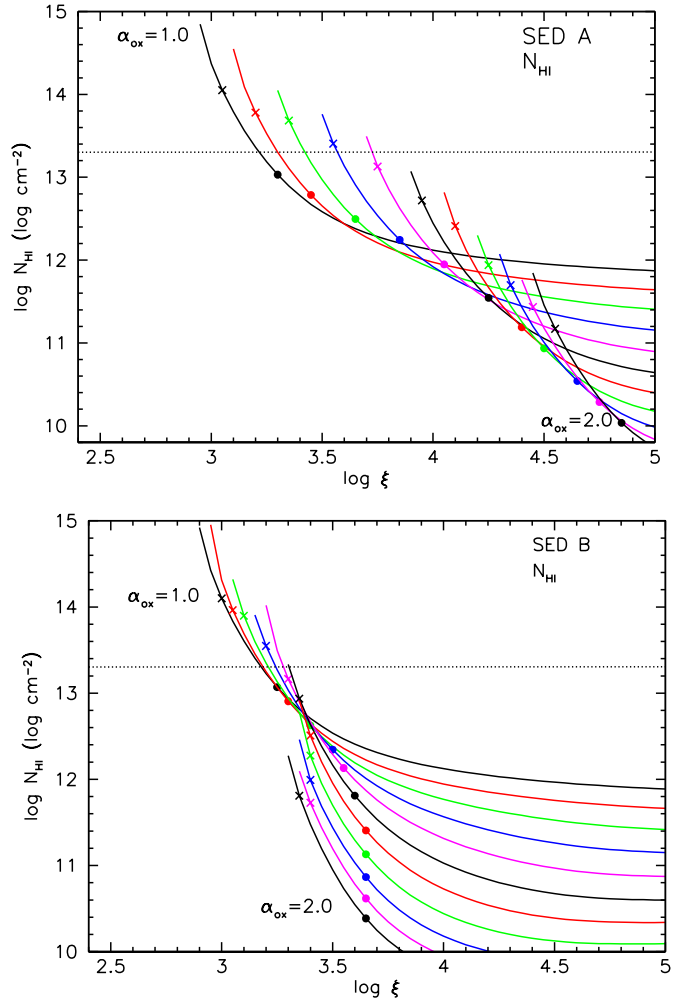


**Figure 7.** : Predicted neutral hydrogen column densities for photoionization models producing Fe XXVI absorption with EW=30 eV. The models in Panel A use SED A with  $\alpha_{\text{ox}}$  ranging from 1.0 to 2.0. The models in Panel B use SED B with  $\alpha_{\text{ox}}$  ranging from 1.0 to 2.0. Solid dots along the curves mark the ionization parameters for which the ionization fraction of Fe XXVI is at a maximum. Crosses give the peak ionization fraction for Fe XXV.

## 6. DISCUSSION

The discovery of H I Ly $\alpha$  absorption associated with the  $v_{\text{out}} = -17300 \text{ km s}^{-1}$  X-ray UFO in the quasar PG 1211+143 offers the prospect of additional spectral diagnostics for studying these energetic phenomena. Such an additional spectral line in a completely different waveband permits a more detailed assessment of the shape of the overall ionizing spectrum and the ionization parameter of the gas in the outflow. Our search for Ly $\alpha$  counterparts in a large sample of X-ray UFOs sets some fairly stringent upper limits on the presence of H I in these fast outflows.

From our large grid of photoionization models and our lack of Ly $\alpha$  absorption detections, we can conclude that either the UFOs in this study are infrequently present, or that their ionization parameters are high. If the X-ray absorption features detected by Tombesi et al. (2010)

**Table 4:** Predicted H I Column Densities for X-ray UFOs in Fe XXVI

Object	EW (eV)	$\log N_{\text{H}}$ ( $\log \text{cm}^{-2}$ )	$\alpha_{ox}$	$\xi_{peak-A}$ ( $\log \text{cm}^{-2}$ )	$\xi_{peak-B}$	$\log N_{\text{HI-A}}$	$\log N_{\text{HI-B}}$
1H0419-577	55	22.99	1.24	3.64	3.38	12.78	12.91
Ark 120	25	22.65	1.32	3.84	3.48	12.16	12.26
Mrk 79	43	22.88	1.40	4.04	3.54	12.12	12.30
NGC 4051	96	23.23	1.48	4.25	3.65	12.11	12.23
NGC 4151	28	22.70	1.07	3.44	3.30	12.75	12.87
	32	22.75	1.07	3.44	3.30	12.82	12.94
PG 1211+143	130	23.36	1.47	4.25	3.65	12.27	12.40
Mrk 766	39	22.84	1.38	4.04	3.54	12.07	12.26
Mrk 205	50	22.95	1.13	3.44	3.30	13.02	13.15
Mrk 279	73	23.11	1.19	3.64	3.38	12.92	13.05
Mrk 841	46	22.91	1.36	4.04	3.54	12.15	12.33
Mrk 290	85	23.18	1.31	3.90	3.48	12.62	12.84
Mrk 509	32	22.75	1.31	3.84	3.48	12.27	12.37
	19	22.53	1.31	3.84	3.48	12.04	12.14
	19	22.53	1.31	3.84	3.48	12.04	12.14
MR2251-178	32	22.75	1.14	3.44	3.30	12.82	12.94

**Notes.** (1) Object name. (2) Equivalent width of the UFO. (3) Total hydrogen column density required to produce a feature of that EW at the peak ion fraction. (4)  $\alpha_{ox}$  for the object. (5) Ionization parameter required to achieve peak ion fraction given  $\alpha_{ox}$  for SED A. (6) Ionization parameter required to achieve peak ion fraction given  $\alpha_{ox}$  for SED B. (7) Predicted H I column density for parameters corresponding to SED A. (8) Predicted H I column density for parameters corresponding to SED B.

**Table 5:** Predicted H I Column Densities for X-ray UFOs in Fe XXV

Object	EW (eV)	$\log N_{\text{H}}$ ( $\log \text{cm}^{-2}$ )	$\alpha_{ox}$	$\xi_{peak-A}$ ( $\log \text{cm}^{-2}$ )	$\xi_{peak-B}$	$\log N_{\text{HI-A}}$	$\log N_{\text{HI-B}}$
1H0419-577	55	22.67	1.24	3.34	3.10	13.29	13.46
Ark 120	25	22.33	1.32	3.54	3.18	12.64	12.80
Mrk 79	43	22.56	1.40	3.74	3.26	12.60	12.88
NGC 4051	96	22.91	1.48	3.95	3.35	12.61	12.84
NGC 4151	28	22.38	1.07	3.15	3.05	13.32	13.31
	32	22.44	1.07	3.16	3.05	13.39	13.37
PG 1211+143	130	23.05	1.47	3.95	3.35	12.77	13.00
Mrk 766	39	22.52	1.38	3.74	3.26	12.55	12.83
Mrk 205	50	22.63	1.13	3.16	3.05	13.59	13.57
Mrk 279	73	22.80	1.19	3.34	3.10	13.42	13.60
Mrk 841	46	22.59	1.36	3.74	3.26	12.63	12.91
Mrk 290	85	22.86	1.31	3.54	3.18	13.21	13.37
Mrk 509	32	22.44	1.31	3.54	3.18	12.75	12.91
	19	22.21	1.31	3.54	3.18	12.52	12.67
	19	22.21	1.31	3.54	3.18	12.52	12.67
MR2251-178	32	22.44	1.14	3.16	3.15	13.39	13.39

**Notes.** (1) Object name. (2) Equivalent width of the UFO. (3) Total hydrogen column density required to produce a feature of that EW at the peak ion fraction. (4)  $\alpha_{ox}$  for the object. (5) Ionization parameter required to achieve peak ion fraction given  $\alpha_{ox}$  for SED A. (6) Ionization parameter required to achieve peak ion fraction given  $\alpha_{ox}$  for SED B. (7) Predicted H I column density for parameters corresponding to SED A. (8) Predicted H I column density for parameters corresponding to SED B.

and Gofford et al. (2013) are produced by Fe XXVI, as shown in Table 4 and Figure 7, the predicted H I column density falls below our upper limits for all objects. However, if the X-ray absorption is produced by Fe XXV, as illustrated by Table 5 and Figure 8, in many cases we would have expected to see Ly $\alpha$  absorption if Fe XXV was near peak ionization. Thus we conclude that it is more likely that the X-ray absorption features are produced by Fe XXVI. Furthermore, ionization parameters for a wide range of models then needs to be higher than  $\log \xi=3.2$ , or Ly $\alpha$  absorption could be produced at detectable levels at below-peak ionization fractions for Fe XXVI if the column density is high enough, e.g.,  $> 5 \times 10^{23} \text{ cm}^{-2}$ . Such high ionization parameters are generally expected based on the photoionization models

and fits to the X-ray spectra performed by Tombesi et al. (2011) and Gofford et al. (2013), but this study does provide independent confirmation.

Our analysis above has rested on assuming that the UFO-producing gas has large turbulent velocities,  $\gtrsim 1000 \text{ km s}^{-1}$ , rendering it optically thin. If the UFO features do have intrinsic widths of only 100-200  $\text{km s}^{-1}$ , as in the lower-ionization UFO in PG 1211+143 at  $v_{out} = -17300 \text{ km s}^{-1}$  (Danehar et al. 2018), then the required total column densities to produce the Fe absorption would be significantly higher (see the curves of growth in Tombesi et al. 2011), and the corresponding predictions for H I would also be higher. That would then lead to the prediction that Ly $\alpha$  features would be even easier to detect, making it surprising that we do not

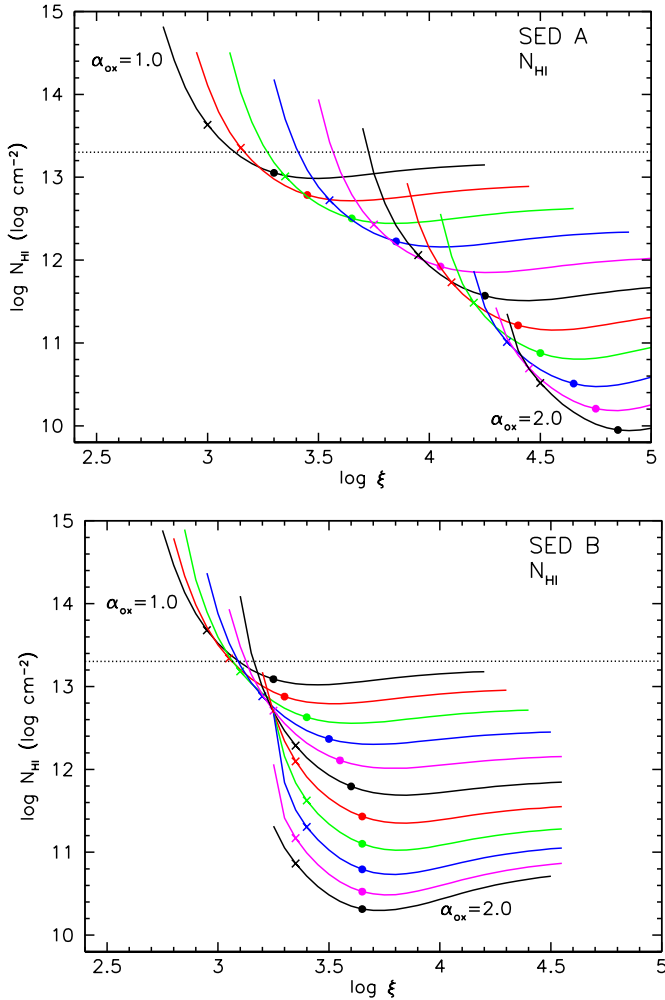


**Figure 8.** : Predicted neutral hydrogen column densities for photoionization models producing Fe XXV absorption with EW=30 eV. The models in Panel A use SED A with  $\alpha_{ox}$  ranging from 1.0 to 2.0. The models in Panel B use SED B with  $\alpha_{ox}$  ranging from 1.0 to 2.0. Solid dots along the curves mark the ionization parameters for which the ionization fraction of Fe XXV is at a maximum. Crosses give the peak ionization fraction for Fe XXV.

find a significant number.

Another interesting way to explore our photoionization models is to approach them from the reverse direction, and investigate what range of physical conditions can produce strong Ly $\alpha$  absorption as seen by Kriss et al. (2018). Figures 9 and 10 show column densities for the primary UV and X-ray ions we have been investigating as a function of ionization parameter for photoionization solutions that would produce a neutral hydrogen column density of  $\log N_{\text{HI}} = 14.29 \text{ cm}^{-2}$ . The top panel in each figure shows the total column density associated with those models. Such a neutral hydrogen column would produce a Ly $\alpha$  absorption line with FWHM = 1000 km s $^{-1}$ , comparable to the strength of the Ly $\alpha$  absorption in PG 1211+143, and the fiducial model we show in the spectra in Figure 1. As in Figures 5 and 6, C IV, N V and O VI are typically undetectable if  $\log N_{\text{ion}} < 13.0 \text{ cm}^{-2}$ , a 30-eV EW feature in Fe XXV or

Fe XXVI requires  $\log N_{\text{ion}} = 17.57$  and 17.84, respectively, and O VIII and Ne X are visible only with column densities  $\log N_{\text{ion}} > 17.4 \text{ cm}^{-2}$ .

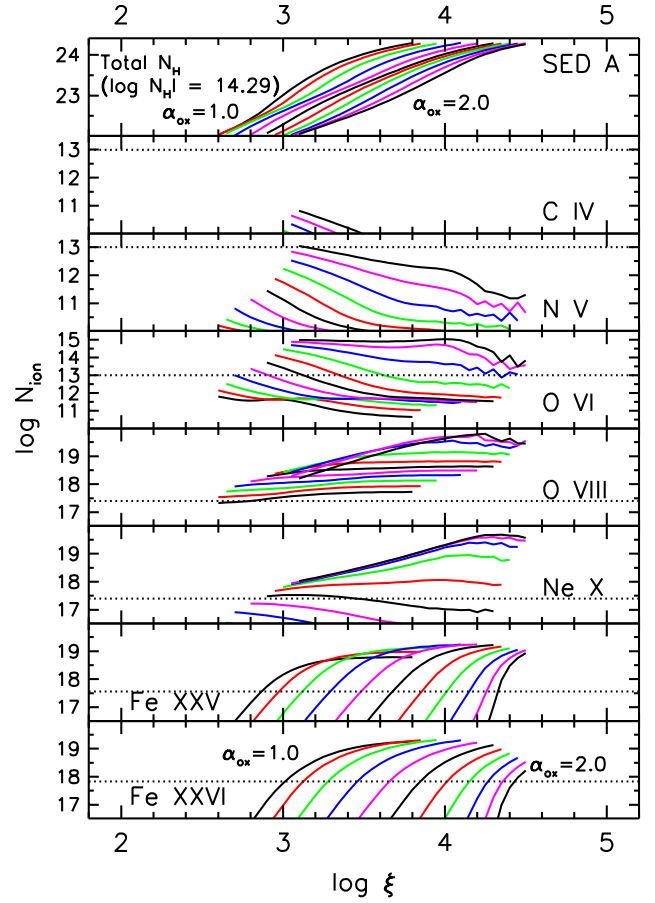


**Figure 9.** : Ionic column densities as a function of ionization parameter for SED A that correspond to an ionization model solution that produces a 1-Å EW Ly $\alpha$  absorption line. With a FWHM = 1000 km s $^{-1}$ , such a line has a neutral hydrogen column density of  $\log N_{\text{HI}} = 14.29 \text{ cm}^{-2}$ . The alternating color curves span a range in  $\alpha_{ox}$  from 1.0 to 2.0 at intervals of 0.1. Dashed horizontal lines show approximate thresholds for each ion for detecting UV or X-ray absorption lines (see text).

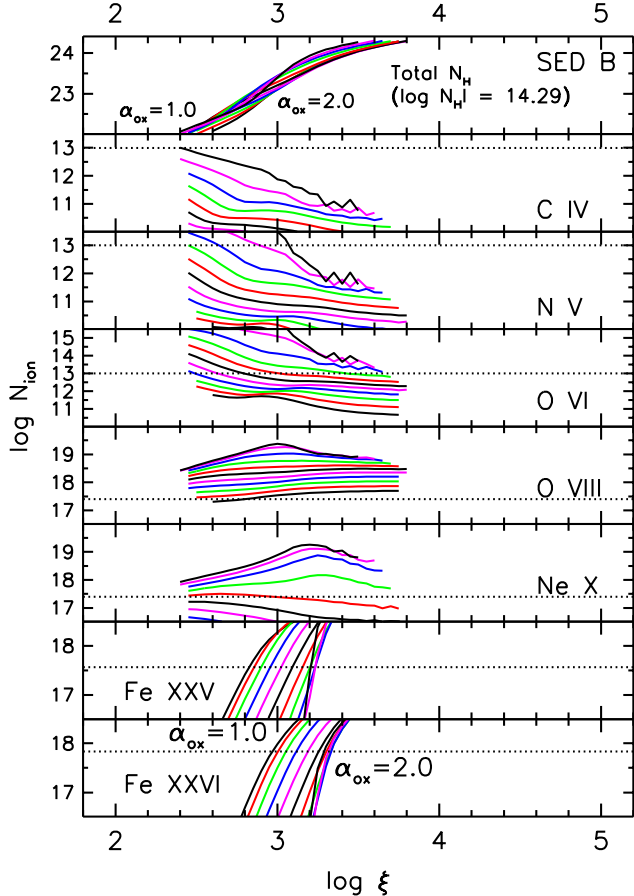


**Figure 10.** : Ionic column densities as a function of ionization parameter for SED B that correspond to an ionization model solution that produces a 1-Å EW Ly $\alpha$  absorption line. With a FWHM = 1000 km s $^{-1}$ , such a line has a neutral hydrogen column density of  $\log N_{\text{H}} = 14.29$  cm $^{-2}$ . The alternating color curves span a range in  $\alpha_{\text{ox}}$  from 1.0 to 2.0 at intervals of 0.1. Dashed horizontal lines show approximate thresholds for each ion for detecting UV or X-ray absorption lines (see text).

If we look at predicted column densities for an ionization parameter  $\log \xi = 3.0$  and  $\alpha_{\text{ox}} = 1.5$ , comparable to the conditions in PG 1211+143, one sees that the total column density is  $\log N_{\text{H}} \sim 10^{22}$  cm $^{-2}$ , C IV and N V are invisible and O VI is possibly detectable at a few  $\times 10^{13}$  cm $^{-2}$ . In the X-ray, O VIII and Ne X should be seen in a good grating spectrum, but the ionization level is too low to produce detectable Fe XXV or Fe XXVI features.

At slightly higher ionization parameters, C IV and N V remain undetectable, and O VI is strong only for soft spectra with high  $\alpha_{\text{ox}}$ . However, O VIII and Ne X increase in strength, and they should produce easily identifiable features in X-ray grating spectra. Fe XXV and Fe XXVI do not become detectable until  $\log \xi > 3.6$ . So, in the case of a strong UV H I Ly $\alpha$  feature in which Fe XXV and Fe XXVI are also detected, one should also see strong intermediate ionization ions such as O VIII

and Ne X. Again, we must conclude that strong H I Ly $\alpha$  absorption should be accompanied by other spectral features in addition to Fe XXV or Fe XXVI.

In the more specific case of Mrk 79, although our detection of Ly $\alpha$  is tentative, evaluating its implications is instructive. Since we know the overall SED of Mrk 79, we can more specifically determine what ionization parameter will produce both Fe XXVI and H I, instead of examining a full grid of possibilities as in Figure 7. First we note that Figures 7 and 8 show that the X-ray absorption feature must be Fe XXV in order to produce the observed column density of neutral hydrogen. Therefore, Figure 11 shows curves similar to those in Figure 7, but specifically computed for  $\text{EW} = 43 \pm 18$  eV as reported by Tombesi et al. (2010) with  $\alpha_{\text{ox}} = 1.4$  and SED A. The enclosed area then intersects the observed H I column density error region at only at the extreme lower limits for the ionization parameter,  $\log \xi = 3.55$ , significantly below peak ion fraction for Fe XXV, and well below the peak for Fe XXVI. The implied total hydrogen column for this model has  $\log N_{\text{H}} = 4.2 \times 10^{23}$  cm $^{-2}$ . This case illustrates that detectable H I is possible if the Fe ionization fraction is considerably below peak. Tombesi et al. (2011) give  $\log \xi = 4.19 \pm 0.19$  and  $N_{\text{H}} = (1.94 \pm 1.2) \times 10^{23}$  cm $^{-2}$ , which is a higher ionization parameter than necessary for producing detectable H I, but we also note that the SED used in their photoionization model has an extraordinarily high X-ray to optical luminosity ratio, with  $\alpha_{\text{ox}} = 1$ . However, our tentative solution of very high column density and lower ionization parameter is problematic since it lies at such an extreme location in parameter space. In addition, as shown in Figure 9, lower-ionization X-ray species such as O VIII and Ne X should also be present, and they are not. If the UFO was present at the time of the UV observations, it looked significantly different in total column density and ionization than as reported in Tombesi et al. (2011).

Variability is a potential explanation for these discrepancies. Gallo et al. (2011) show that Mrk 79 exhibits significant variations in X-ray flux both in the hard band (3–10 keV), where variations of factors of 2–3 are common, and up to ten-fold variations in flux at low energy,  $< 1$  keV. The UFO reported by Tombesi et al. (2010) corresponds to a high flux state of Mrk 79. The *FUSE* observations of Mrk 79 precede the first two *XMM-Newton* observations by 10–14 months. Both of these X-ray observations are in intermediate to low flux states, factors of 2–10 lower. If these states were comparable to the one at the time of the *FUSE* observations, a low ionization parameter consistent with our possible detection of broad H I would be possible. However, this still leaves open the question why an ultra-fast outflow in intermediate-ionization ions was not observed in a similar low-flux state in 2008. Variability in column density is a possibility, but it may also be true that broad,  $\sim 1000$  km s $^{-1}$  width features would have been hard to detect in the low-flux *XMM-Newton* RGS spectrum.

Producing high column densities of H I associated with Fe XXVI UFOs becomes even more difficult for Ly $\alpha$  absorption features even stronger than the possible feature in Mrk 79 or PG 1211+143. To produce H I column

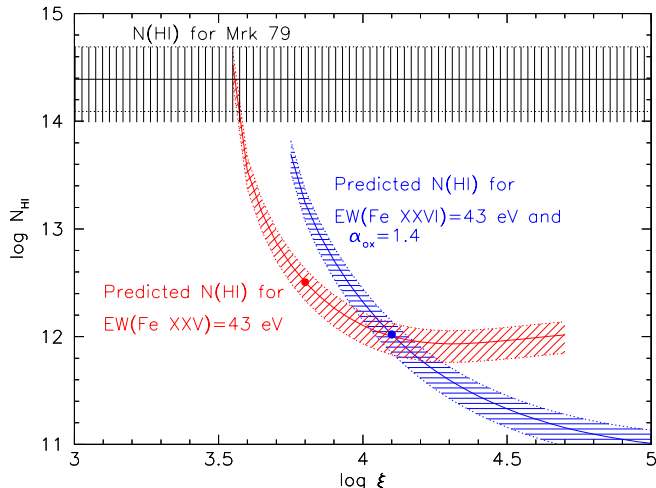


**Figure 11.** : Predicted neutral hydrogen column densities for photoionization models producing Fe XXV or Fe XXVI absorption with  $EW=43 \pm 14$  eV in Mrk 79. The slanting curves show results using SED A for an  $\alpha_{ox} = 1.4$  with the shaded region showing the error bars corresponding to the uncertainty in EW of the X-ray UFO. The horizontal band shows the observed H I column density with  $1\text{-}\sigma$  error bars. The solid dots shows the locations of maximum ionization fraction for Fe XXV and Fe XXVI in the photoionization models.

densities above  $\log N_{\text{H}} > 15.35 \text{ cm}^{-2}$ , as Hamann et al. (2018) investigated as a possibility in PDS 456, ionization parameters must be low and total column densities must be high. This leads to strong ionization fronts in ions well below the ionization of Fe XXV and Fe XXVI, and all the intermediate ionization species we have been investigating (C IV, N V, O VI, O VIII, and Ne X) produce strong spectral features. Hamann et al. (2018) draw the same conclusion, and rule out Ly $\alpha$  absorption at  $v = -0.06c \text{ km s}^{-1}$  as a possible identification for the spectral feature in the 2000 STIS spectrum of PDS 456.

Our evaluation of the non-detection of Ly $\alpha$  counterparts to highly ionized Fe X-ray absorption lines has assumed that the gas producing the Fe absorption as well as the Ly $\alpha$  absorption arises in the same parcel of photoionized gas. However, several authors have suggested that lower-ionization gas might be embedded as denser clumps in the more highly ionized Fe outflows (Longinotti et al. 2015; Hagino et al. 2017; Hamann et al. 2018). In such models, one might expect Ly $\alpha$  absorption to be even more common, as denser, lower-ionization clumps embedded in the UFO would have a greater propensity to produce higher column densities in lower-ionization species such as H I (and C IV, N V, and O VI). Given that we do not detect H I absorption in most cases, it seems likely that co-existing clumps of denser, lower ionization gas, embedded in UFOs is also not a common phenomenon. However, mitigating possibilities to this conclusion would be that the entrained, high-density material does not have the same velocity, or, as we discuss below, variability.

Variability is a confounding factor in interpreting these results. As Kriss et al. (2018) showed, the broad Ly $\alpha$  absorption detected in PG 1211+143 is not always present.

Reeves et al. (2018) also see dramatic variability in the soft X-ray spectrum of the  $v_{out} \sim -18000 \text{ km s}^{-1}$  outflow in PG 1211+143. At the time of their *XMM-Newton* observation it was not only brighter, with higher ionization parameter and higher total column density than that observed by Danehkar et al. (2018) when the Ly $\alpha$  absorption was present, but it also had a strong, low-ionization zone with  $\log \xi = 1.32$  and  $N_{\text{H}} = 1.3 \times 10^{21} \text{ cm}^{-2}$ . This gas would have produced strong, deep UV lines in H I, C IV, N V, and O VI, all of which would have been easily detected in the HST/COS observations of Danehkar et al. (2018) and Kriss et al. (2018). Such dramatic variability means that non-detections and upper limits derived from non-simultaneous observations can represent conditions that differ by orders of magnitude in column density of the outflowing gas. More readily interpreted results require simultaneous UV and X-ray spectra.

## 7. SUMMARY

We have examined 36 archival UV spectra to search for potential H I Ly $\alpha$  absorption counterparts to a sample of 16 X-ray ultra-fast outflows selected from Tombesi et al. (2010) and Gofford et al. (2013). Two FUSE spectra of Mrk 79 show evidence for broad Ly $\alpha$  absorption at the expected wavelength for its UFO, but these detections are tentative since they appear in only one of two simultaneous exposures. This tentative feature has FWHM=910  $\text{km s}^{-1}$ , an equivalent width of 1.3  $\text{\AA}$ , and an implied H I column density of  $2.5 \times 10^{14} \text{ cm}^{-2}$ . If the X-ray UFO has an ionization parameter of  $\log \xi=3.55$  and a total column density of  $N_{\text{H}} = 4.2 \times 10^{23} \text{ cm}^{-2}$ , then the same gas can produce both the H I and the UFO, but the X-ray feature must be Fe XXV and not Fe XXVI. One would also expect to detect lower-ionization species (e.g., O VIII) in the X-ray spectrum of Mrk 79 at the UFO velocity, and they are not present.

Applying a search criterion of a line width of 1000  $\text{km s}^{-1}$ , comparable to the Ly $\alpha$  counterpart to an X-ray UFO in PG 1211+143 discovered by Kriss et al. (2018), we can set upper limits on associated H I column densities in the range from  $\log N_{\text{HI}}=12.7$  to  $14.4 \text{ cm}^{-2}$ , with most having  $\log N_{\text{HI}} < 13.3 \text{ cm}^{-2}$ . We have computed a set of photoionization models covering a large grid of possible SEDs that shows that if most X-ray UFO absorbers are Fe XXV or Fe XXVI near their peak ionization fractions, the associated column densities of H I would be lower than these limits. In general, ionization parameters have to be higher than  $\log \xi=3.7$  to make H I undetectable. Lower ionization parameters can produce detectable UV absorbing gas, however, so an alternative explanation of the paucity of counterparts in our search is that variability only renders them visible on rare occasions, or that the UV ionizing continuum is very hard.

We thank M. Cappi for suggesting this study. All of the data presented in this paper were obtained from the Mikulski Archive for Space Telescopes (MAST). STScI is operated by the Association of Universities for Research in Astronomy, Inc., under NASA contract NAS5-26555.

Support for MAST for non-HST data is provided by the NASA Office of Space Science via grant NNX09AF08G and by other grants and contracts. This work was supported by NASA through grant NNX13AF18G, and by a grant for *HST* program number 13233 from the Space Telescope Science Institute (STScI), which is operated by the Association of Universities for Research in Astronomy, Incorporated, under NASA contract NAS5-26555. This research has made use of the NASA/IPAC Extragalactic Database (NED), which is operated by the Jet Propulsion Laboratory, California Institute of Technology, under contract with the National Aeronautics and Space Administration.

## REFERENCES

- Anglés-Alcázar, D., Faucher-Giguère, C.-A., Kereš, D., et al. 2017, *MNRAS*, 470, 4698
- Arav, N., Gabel, J. R., Korista, K. T., et al. 2007, *ApJ*, 658, 829
- Beckmann, R. S., Devriendt, J., Slyz, A., et al. 2017, *MNRAS*, 472, 949
- Costantini, E., Kaastra, J. S., Arav, N., et al. 2007, *A&A*, 461, 121
- Crenshaw, D. M., & Kraemer, S. B. 2012, *ApJ*, 753, 75
- Crenshaw, D. M., Kraemer, S. B., & George, I. M. 2003, *ARAA*, 41, 117
- Danehkar, A., Nowak, M. A., Lee, J. C., et al. 2018, *ApJ*, 853, 165
- De Rosa, G., Peterson, B. M., Ely, J., et al. 2015, *ApJ*, 806, 128
- Detmers, R. G., et al. 2011, *A&A*, 534, A38
- Di Matteo, T., et al. 2005, *Nature*, 433, 604
- Dixon, W. V., Sahnou, D. J., Barrett, P. E., et al. 2007, *PASP*, 119, 527
- Dubois, Y., Gavazzi, R., Peirani, S., & Silk, J. 2013, *MNRAS*, 433, 3297
- Dunn, J. P., et al. 2008, *AJ*, 136, 1201
- Edmonds, D., et al. 2011, *ApJ*, 739, 7
- Elvis, M., Wilkes, B. J., McDowell, J. C., et al. 1994, *ApJS*, 95, 1
- Faucher-Giguère, C.-A., & Quataert, E. 2012, *MNRAS*, 425, 605
- Faucher-Giguère, C.-A., Quataert, E., & Hopkins, P. F. 2013, *MNRAS*, 433, 1970
- Ferland, G. J., Chatzikos, M., Guzmán, F., et al. 2017, *RMxAA*, 53, 385
- Ferrarese, L., & Merritt, D. 2000, *ApJ*, 539, L9
- Fukumura, K., Kazanas, D., Contopoulos, I., & Behar, E. 2010, *ApJ*, 723, L228
- Gabel, J. R., et al. 2005, *ApJ*, 623, 85
- Gallo, L. C., Miniutti, G., Miller, J. M., et al. 2011, *MNRAS*, 411, 607
- Gebhardt, K., et al. 2000, *ApJ*, 539, L13
- Gofford, J., Reeves, J. N., Tombesi, F., et al. 2013, *MNRAS*, 430, 60
- Green, J. C., Froning, C. S., Osterman, S., et al. 2012, *ApJ*, 744, 60
- Hagino, K., Done, C., Odaka, H., Watanabe, S., & Takahashi, T. 2017, *MNRAS*, 468, 1442
- Hamann, F., Chartas, G., Reeves, J., & Nardini, E. 2018, *ArXiv e-prints*, arXiv:1801.04302
- Hopkins, P. F., & Elvis, M. 2010, *MNRAS*, 401, 7
- Hopkins, P. F., Kereš, D., Oñorbe, J., et al. 2014, *MNRAS*, 445, 581
- Kaastra, J. S., Detmers, R. G., Mehdipour, M., et al. 2012, *A&A*, 539, A117
- King, A. 2003, *ApJ*, 596, L27
- King, A., & Pounds, K. 2015, *ARAA*, 53, 115
- Kraemer, S. B., George, I. M., Crenshaw, D. M., et al. 2005, *ApJ*, 633, 693
- Kraemer, S. B., Crenshaw, D. M., Dunn, J. P., et al. 2012, *ApJ*, 751, 84
- Kriss, G. 1994, *Astronomical Data Analysis Software and Systems*, 3, 437
- Kriss, G. A., Lee, J. C., Danehkar, A., et al. 2018, *ApJ*, 853, 166
- Kriss, G. A., et al. 2000, *ApJ*, 538, L17
- . 2011, *A&A*, 534, A41
- Laha, S., Guainazzi, M., Dewangan, G. C., Chakravorty, S., & Kembhavi, A. K. 2014, *MNRAS*, 441, 2613
- Lee, J. C., Kriss, G. A., Chakravorty, S., et al. 2013, *MNRAS*, 430, 2650
- Longinotti, A. L., Krongold, Y., Guainazzi, M., et al. 2015, *ApJ*, 813, L39
- Mehdipour, M., Branduardi-Raymont, G., Kaastra, J. S., et al. 2011, *A&A*, 534, A39
- Moos, H. W., Cash, W. C., Cowie, L. L., et al. 2000, *ApJ*, 538, L1
- Nardini, E., Reeves, J. N., Gofford, J., et al. 2015, *Science*, 347, 860
- Nelson, D., Genel, S., Vogelsberger, M., et al. 2015, *MNRAS*, 448, 59
- Ostriker, J. P., Choi, E., Ciotti, L., Novak, G. S., & Proga, D. 2010, *ApJ*, 722, 642
- Parker, M. L., Pinto, C., Fabian, A. C., et al. 2017, *Nature*, 543, 83
- Pounds, K., Lobban, A., Reeves, J., & Vaughan, S. 2016, *MNRAS*, 457, 2951
- Pounds, K. A. 2014, *MNRAS*, 437, 3221
- Pounds, K. A., Reeves, J. N., King, A. R., et al. 2003, *MNRAS*, 345, 705
- Pounds, K. A., Reeves, J. N., Page, K. L., & O'Brien, P. T. 2004, *ApJ*, 616, 696
- Reeves, J., Lobban, A., & Pounds, K. 2018, *ArXiv e-prints*, arXiv:1801.03784
- Saez, C., & Chartas, G. 2011, *ApJ*, 737, 91
- Savage, B. D., & Sembach, K. R. 1991, *ApJ*, 379, 245
- Shang, Z., Brotherton, M. S., Green, R. F., et al. 2005, *ApJ*, 619, 41
- Shang, Z., Brotherton, M. S., Wills, B. J., et al. 2011, *ApJS*, 196, 2
- Silk, J., & Rees, M. J. 1998, *A&A*, 331, L1
- Soker, N. 2010, *MNRAS*, 407, 2355
- Telfer, R. C., Zheng, W., Kriss, G. A., & Davidsen, A. F. 2002, *ApJ*, 565, 773
- Thompson, T. A., Fabian, A. C., Quataert, E., & Murray, N. 2015, *MNRAS*, 449, 147
- Tilton, E. M., Danforth, C. W., Shull, J. M., & Ross, T. L. 2012, *ApJ*, 759, 112
- Tombesi, F., & Cappi, M. 2014, *MNRAS*, 443, L104
- Tombesi, F., Cappi, M., Reeves, J. N., et al. 2013, *MNRAS*, 430, 1102
- . 2011, *ApJ*, 742, 44
- Tombesi, F., Meléndez, M., Veilleux, S., et al. 2015, *Nature*, 519, 436
- Tombesi, F., Tazaki, F., Mushotzky, R. F., et al. 2014, *MNRAS*, 443, 2154
- Tombesi, F., Veilleux, S., Meléndez, M., et al. 2017, *ApJ*, 850, 151
- Tombesi, F., et al. 2010, *A&A*, 521, A57
- Woodgate, B. E., Kimble, R. A., Bowers, C. W., et al. 1998, *PASP*, 110, 1183
- Zhang, S. N., Ji, L., Kallman, T. R., et al. 2015, *MNRAS*, 447, 2671
- Zhang, S. N., Ji, L., Marshall, H. L., et al. 2011, *MNRAS*, 410, 2274
- Zheng, W., Kriss, G. A., Telfer, R. C., Grimes, J. P., & Davidsen, A. F. 1997, *ApJ*, 475, 469
- Zubovas, K., & Nayakshin, S. 2014, *MNRAS*, 440, 2625

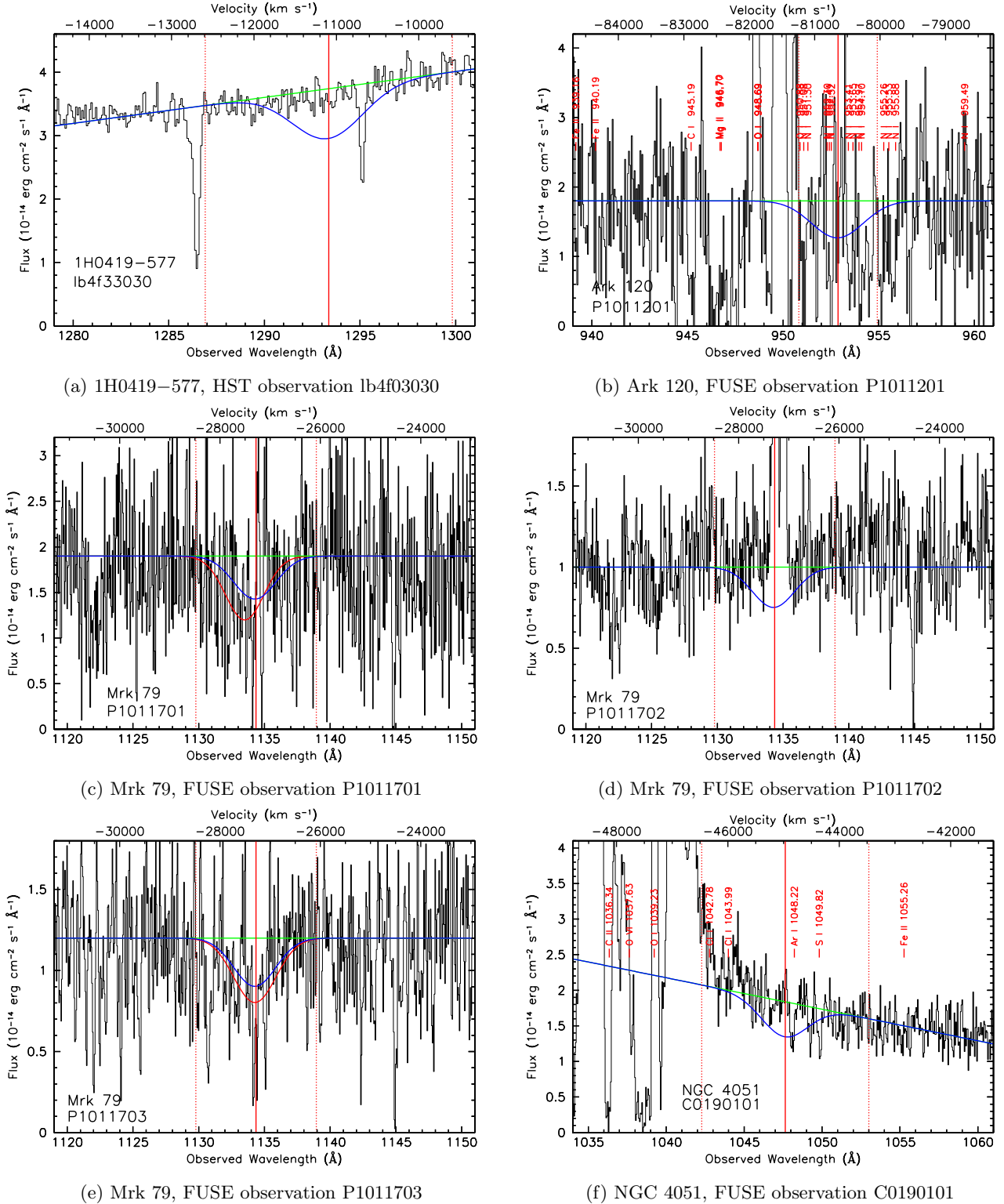
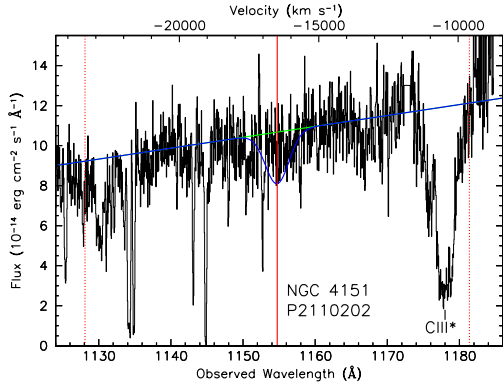
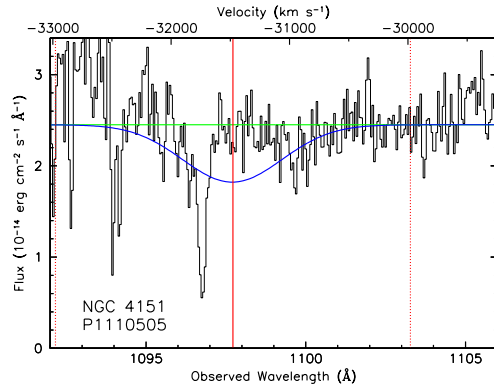


**Figure 1.** : FUSE and HST spectra of regions surrounding the predicted positions of Ly $\alpha$  counterparts to X-ray UFOs. A thin red vertical line marks the predicted wavelength, and the two red vertical dashed lines gives the error region for the prediction. The lower horizontal scale gives the observed wavelength. The upper horizontal scale gives the outflow velocity in km s $^{-1}$ . The green line gives the fitted continuum at the location of predicted Ly $\alpha$ . The blue line shows the best fit, incorporating additional emission and absorption components as needed for each object. In addition, the blue line illustrates the predicted appearance of a 1  $\text{\AA}$  EW absorption line with FWHM=1000 km s $^{-1}$  at the predicted position of Ly $\alpha$ . Red lines in Figures 1c and 1e for Mrk 79 show the best fit for detected Ly $\alpha$  absorption lines. For some spectra, interstellar absorption lines are labeled in red.

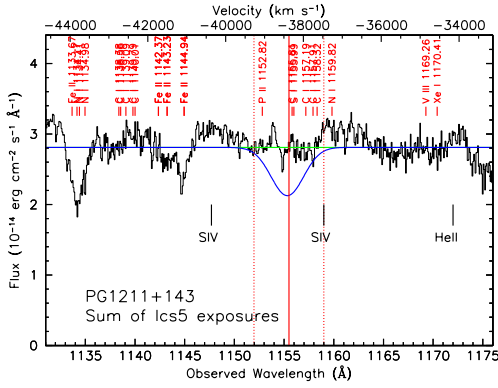




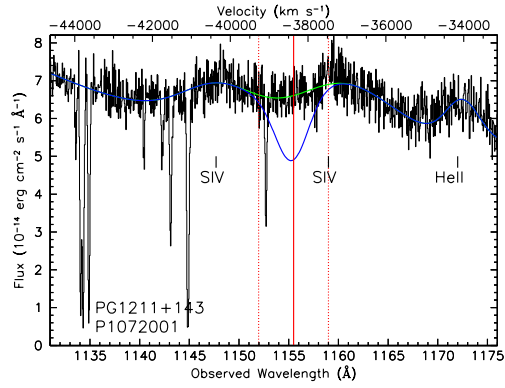
(g) NGC 4151, FUSE observation P2110202



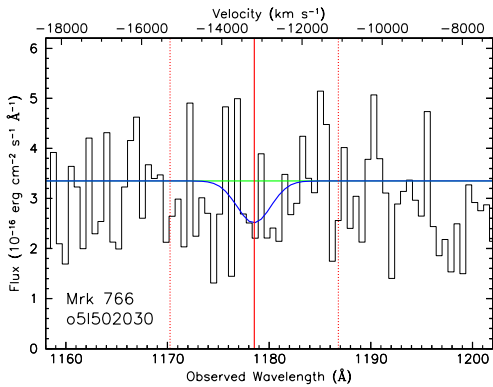
(h) NGC 4151, FUSE observation P1110505



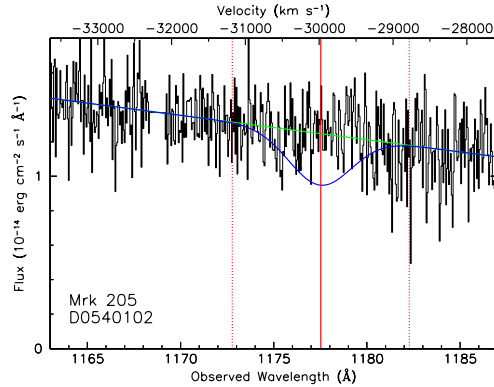
(i) PG 1211+143, Sum of HST observations lcs501010, lcs502010, and lcs504010



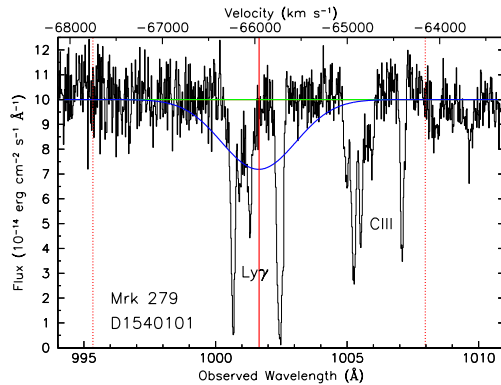
(j) PG 1211+143, FUSE observation P1072001



(k) Mrk 766, HST observation o51502030

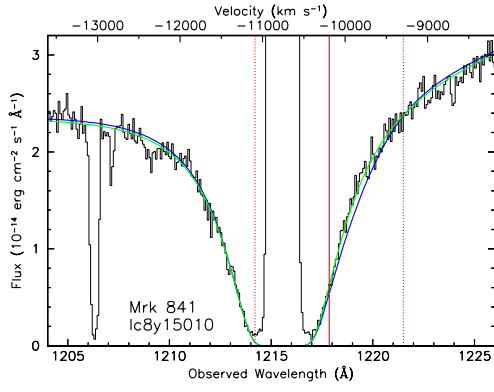


(l) Mrk 205, FUSE observation D0540102

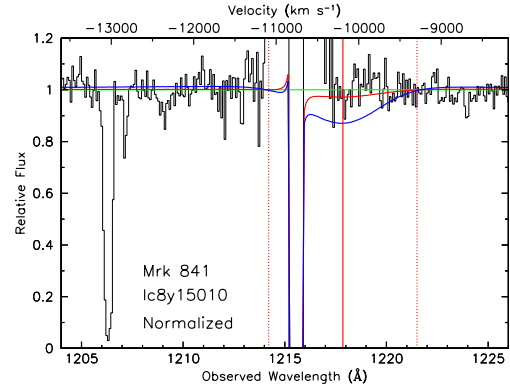
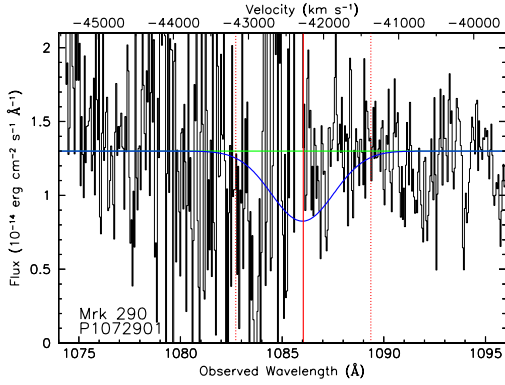


(m) Mrk 279, FUSE observation D1540101. Intrinsic absorption in Ly $\gamma$  and C III  $\lambda$ 977 are marked.

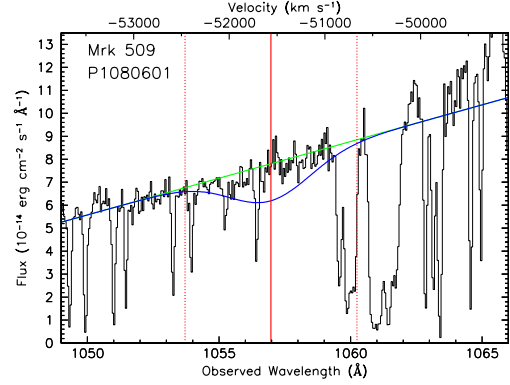
Figure 1. : (cont.)



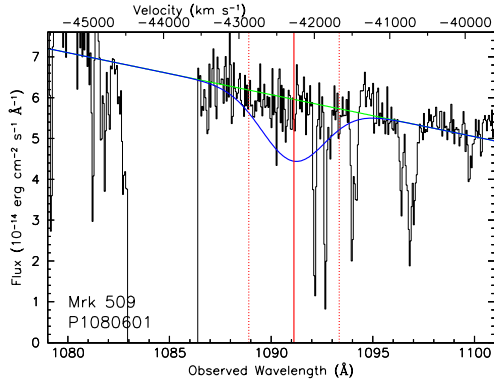
(n) Mrk 841, HST observation lc8y15010

(o) Mrk 841, normalized best-fit spectrum. The red line shows the  $2\sigma$  upper limit.

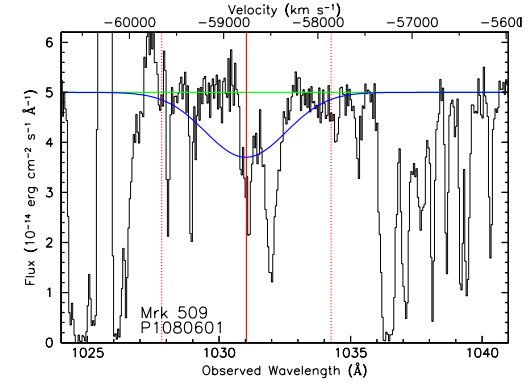
(p) Mrk 290, FUSE observation P1072901



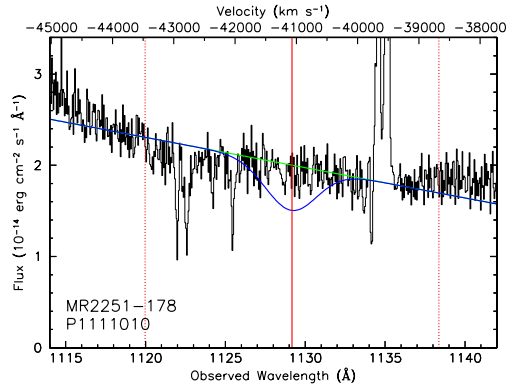
(q) Mrk 509, FUSE observation P1080601



(r) Mrk 509, FUSE observation P1080601



(s) Mrk 509, FUSE observation P1080601



(t) MR2251-178, FUSE observation P1111010

Figure 1. : (cont.)